Review

Chinedu I. Ossai* and Nagarajan Raghavan*

Nanostructure and nanomaterial characterization, growth mechanisms, and applications

https://doi.org/10.1515/ntrev-2017-0156
Received June 26, 2017; accepted August 19, 2017; previously published online November 27, 2017

Abstract: Nanostructures are playing significant roles in the development of new functions and the enhancement of the existing functions of industrial devices such as sensors, transistors, diodes, lithium-ion batteries, and photovoltaic cells, due to their piezoelectricity, biocompatibility, and pyroelectrical characteristics. This research focused on the review of the characteristics of different nanostructures and nanomaterials such as ZnO, ZnS, MoS_2, GO, TiO_2, SnO_2, and Fe_2O_3, their fabrication techniques, growth mechanisms, and applications. The factors affecting the growth mechanisms, the crystallographic natures, growth models of anisotropic nanostructures, and growth of nanocrystals, were also highlighted in this research. The existence of lattice mismatch, differential thermal expansion, and high deposition temperature, have affected uniform deposition of nanoparticles on substrates and caused heteroepitaxy, which has resulted in defective nanostructures. Although heteroepitaxy has negatively affected the characteristics and potential applications of nanostructures, it has also opened new research frontiers for potential new applications of nanostructures. The use of nanostructures for gas sensing is attributed to the high specific area, change of resistance on exposure to gases, and high photoconduction abilities, while the photon-carrier collection abilities and anti-reflectance qualities are vital for solar photovoltaic cells. Nanostructures have also been used as coating pigments to prevent corrosion of facilities, reduce urban heat islands and energy consumptions, due to the near-infrared (NIR) reflective characteristics.

Keywords: anisotropic growth models; crystallographic nature; growth mechanisms; heteroepitaxy; nanofabrication processes; nanostructures characteristics.

***Corresponding authors: Chinedu I. Ossai and Nagarajan Raghavan,** Engineering Product Development Pillar, Singapore University of Technology and Design, Singapore 487372, Singapore, e-mail: chinedu_ossai@sutd.edu.sg (C.I. Ossai); nagarajan@sutd.edu.sg (N. Raghavan)

1 Introduction

The advances in nanotechnology over the years have made nanostructures potential targets of the industries, due to their unique characteristics that influence the physical, chemical, electrical, and optoelectrical attributes of nanomaterials. The band gap, high exciton binding energy, piezoelectricity, biocompatibility, and pyroelectrical characteristics of nanomaterials such as ZnO, TiO_2, SnO_2, and Fe_2O_3 have made them suitable for innovative sensors, anodes for lithium-ion batteries, photoanodes, and nanogenerators for electricity harvesting [1–5]. Nanostructures such as nanowires, nanotubes, nanobelts, nanosprings, nanoribbons, nanorings, nanosheets, and nanoparticles have found applications in non-linear optical devices, flat panel displays, light-emitting diodes, lasers, logic gates, and transistors [6, 7]. These nanostructures have been able to acquire their distinctive characteristics via modifications in the morphology, sizes, and shapes, through the fabrication process that involves the application of temperature, pressure, and chemicals such as catalysts and substrates [8]. Hence, the influence of temperature and pH on a one-dimensional (1-D) polymer nanostructure can modify the material, to make it useable in drug delivery, electronic and optical devices, as well as a catalyst and support for fabricating other nanostructures [7, 9–12].

Fabrication of nanomaterials has been done by different physical, chemical, and mechanical methods that used temperature, pressure, and phase transformation to create nanostructures that have greatly enhanced devices, due to their revolutionized electronic, magnetic, optoelectrical, and sensing capabilities [13]. Different fabrication techniques such as wet chemical, physical vapor deposition, molecular beam epitaxy, pulsed laser deposition, sputtering, metal organic deposition, electrode position, and electrospinning have predominated the nanostructures' fabrication, to date [14–16]. However, there remain different problems such as the presence of defects in the nanostructures, due to lattice mismatch that is caused by heteroepitaxy in the fabrication process [17, 18]. This problem and others such as cost, poor throughput, non-uniformity of nanostructure, and risk, have impacted the

fabrication of nanostructures, despite the improvements in their characteristics. Moreover, heteroepitaxial growth of nanostructures and nanocrystals has been associated with a strain relief mechanism that can result in surface reconstruction, step bunching, faceting, and formation of lattice mismatch, which causes misfit dislocations [17]. Despite the improvements achieved in solving the problem of heteroepitaxy via fabrication of nanostructures at low temperature, with buffer layers that can help in the distribution of the defects on the substrates, and the positive impacts of doping and reorientation of geometry [18–21], the nanostructures' growth defect still stands as the most difficult problem of nanoscience. As the defects on the nanostructures affect their characteristics because of the non-uniformity of the distribution of the nanoparticles on the nanofabrication substrates [22], experts are consistently working out new techniques of fabricating nanostructures, to ensure that the defects are minimal. To this end, some researchers have utilized novel fabrication techniques to affect the optical emission characteristic of ZnS nanowires [8], whereas the growth orientation of Silicon (Si) nanowires has been used to influence the optical and electrical characteristics of semiconductor devices developed with them [13]. Similarly, the band gap, electrical conductance, and mechanical properties have also been reported to vary in nanowires that were fabricated with the same techniques but have different growth orientations [13, 23–26]. Furthermore, varying the synthesis times in the fabrication process has also been used to reduce the defects in the nanostructures [27], but the problems associated with growth defects have not allowed researchers to fully tap the potentials of nanostructures; hence, the furtherance of research in this area.

The aspect ratio has been shown to favor nucleation reactions and the formation of nanocrystals [28] that are fundamental to the enhanced characteristics of nanostructures. This characteristic has favored the development of periodic nanostructures for photonic crystals, gratings, and light-trapping structures, which have enhanced anti-reflectance that have been used in photovoltaic cells [29]. The aspect ratio, orientation, chemical composition, and surface energy at the nanostructure interfacial lattices and facets have made the materials to have low thermal conductivity [28–30], a quality that is vital for thermoelectric devices and batteries with greater energy density.

The objective of this study is to review the functional characteristics, growth mechanisms, and the industrial applications of some common anisotropic nanostructures such as nanocombs, nanorings, nanohelixes, nanosprings, nanobelts, nanowires, and nanocages that are obtained from predominant nanomaterials such as ZnO, ZnS, SnO_2, ZnTe, TiO_2, and polymer hybrid materials. We also aim to show the fundamental problems that have dogged experts working with nanostructures, to give insights to potential new areas of nanostructure research, while highlighting the current applications and emerging applications of nanostructures and nanomaterials. The models for growth mechanisms, factors affecting the growth mechanisms, and characteristics of the different nanofabrication processes were also reviewed. It is expected that this work will be a snapshot on the advances in nanostructure and nanomaterial technology and a compendium for guiding future research.

2 Crystallographic nature of nanostructures

The crystallographic nature of nanostructures has been fundamental to the qualities and characteristics that is exhibited by different nanostructures [31]. The nucleation process, reaction of molecules, and crystallization of nanoparticles have been attributed to the structure of different nanomaterials used in the industry today, hence, the need for understanding the crystallographic nature of nanomaterials. Anisotropic bonding in crystallographic structures have been attributed to the 1-D nanostructures of many solid materials [32] because it forms the building blocks of the nanostructures in the nanofabrication process. Research has shown that surface bonding dominates the anisotropic growth of ZnO nanoparticles [33, 34], which forms different pyramidal nanostructures and morphologies at the critical bond length [35]. Again, the existence of the unique symmetric atomic crystalline structures, in solid state atomic lattice, has been attributed to the directional bonding interaction that have resulted in the formation of different 3-D structures that exhibit different chemical, physical, and mechanical characteristics [36]. Anisotropic nanoparticles have also interacted at nanoscale to aid directional bonding, by the exchange of valences [36] and directional selective functionalization of particles, with the resultant geometric re-orientation of nanostructures [36–38].

2.1 ZnS structures and characteristic

ZnS, as an important semiconductor material with high index of refraction and transmittance in visible range, has been a fundamental material in nanostructures,

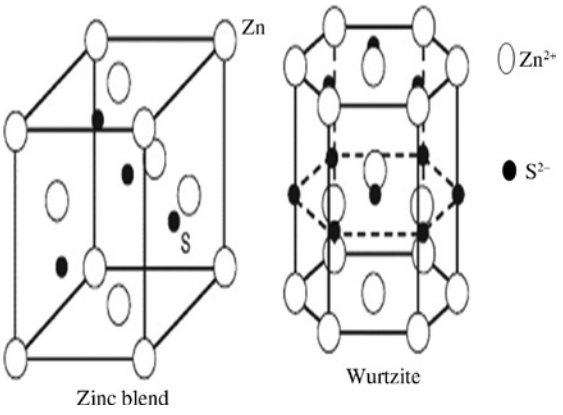

Figure 1: Geometrical structure of ZnS showing the zinc-blended and the wurtzite-blended structure of ZnS nanostructure (Reprinted with permission from Ref. [31], copyright 2006 by the Royal Society of Chemistry).

such as nanowire, nanohelics, nanobelts, and nanocombs [31, 39]. The physical nature of ZnS 1-D nanostructure, synthesized with the vapor-solid process (VSP) was studied by some researchers to understand the polar surface of the growth phenomenon of the material [30, 31]. They showed that the crystallographic structure of ZnS has zinc-blended crystals at room temperature that transforms at a temperature of 1020°C from zinc blended to the hexagonal crystal structure known as wurtzite (Figure 1) [30, 31, 40]. Wurtzite has hexagonal unit cells of alternating tetrahedral coordinates of S^{2-} and Zn^{2+} ions that are packed along one axis and causes the non-centrosymmetric and piezoelectrical characteristics of ZnS nanostructures [31].

The alternating positive and negative charges of Zn^{2+} and S^{2-} in the ZnS crystalline structure resulted in the polarized surfaces-{2110}, {0110}, and ±{001} that contribute to the dipolar and surface energy divergence [31] that may bring about asymmetric growth of the ZnS nanostructures, during the nanofabrication process. The surface polarity, surface energy of the crystalline planes, and chemical activities on the crystalline planes have been the major contributors to anisotropic growth of the ZnS nanostructures (Figure 2) [31].

It has also been shown that the ZnS nanostructures are dependent on the substrate temperature and the catalyst used for their fabrication [39]. It was evident that different nanostructures of ZnS such as nanorods, nanowires, nanobelts, and nanosheets can be obtained with varying characteristics, when the temperature and catalysts were alternated, hence, providing a significant insight into the ZnS nanostructure shape, size, and morphological orientation [39]. This is a step that is vital for controlling the design and development of the new ZnS nanostructures and their applications.

2.2 ZnO structures and characteristic

ZnO is one of the nanomaterials that have found widespread application due to the surface and quantum confinement effects, which have made them show novel electrical, chemical, mechanical, and optical properties. These properties have usefulness in field effect transistors, resonators, sensors, and nanocantilevers [30]. ZnO has a wide band gap of 3.37 eV [30, 41–43], and the strong piezoelectric and pyroelectric properties caused by the lack of

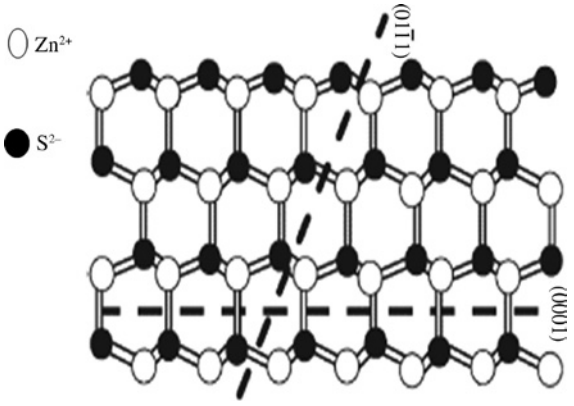

Figure 2: ZnS wurtzite polar crystalline nanostructure projected along [1210] (Reprinted with permission from Ref. [31], copyright 2006 by the Royal Society of Chemistry).

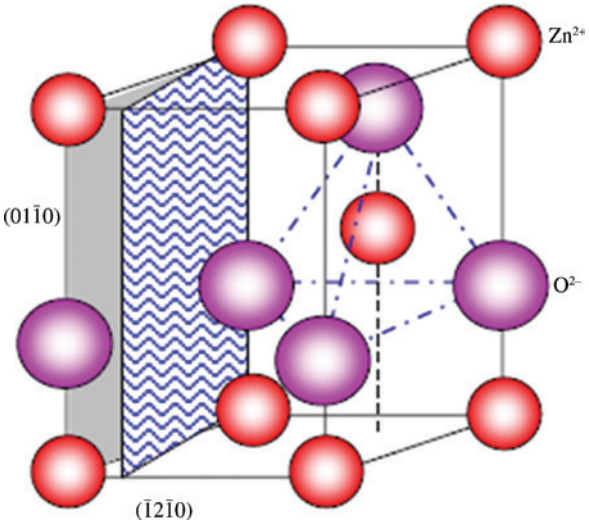

Figure 3: ZnO wurtzite structure showing the polarities (Reprinted with permission from Ref. [30], copyright 2004 by IOP Publishing).

central symmetry of the wurtzite (Figure 3) [41, 44] makes it suitable for short-wavelength optoelectronic application [41, 42]. The piezoelectric and pyroelectric properties make the material suitable for sensors, transducers, energy generators, and photo-catalysts for hydrogen production, while the biocompatibility and nontoxic characteristics make it suitable for medicine [41]. The high exciton-binding energy of 60 meV in the ZnO crystals [42, 44–46] ensures efficient excitonic emission at room temperature [42], whereas the transparency to visible light makes the material extremely conductive after doping. The ZnO nanostructure has a polar characteristic that is dominated with a basal plane and other planes that include ZnO ± {0001} that is atomically flat, stable, and without reconstruction, ZnO $\{2\bar{1}\bar{1}0\}$, and ZnO $\{01\bar{1}0\}$ that are non-polar surfaces with lower energy than {0001} facets [41].

Per previous study in Ref. [47] carried out at 860°C using vapor transport deposition (VTD), under similar growth conditions, ZnO nanostructures can be switched between {0001} – axial nanowire and $\{11\bar{2}0\}$ – axial nanobelt, by adding indium to the source. The research showed that the nanowires were observed as ordered vertical arrays of pure ZnO, whereas the nanobelts had no spatial ordering. Fan et al. [47] concluded that the crystallographic orientation of the nanobelts were influenced by the dissolution of the indium ion into the Au (used as a template) during the nucleation of the ZnO at the solid-liquid interface. It was also affirmed by these researchers that the doped nanobelt have a higher photon-carrier concentration than the nanowire, after using photoluminescence and resonant Raman scattering technique to characterize the materials.

ZnO is a polar-dominated nanostructure that is centrally constituted of nanowires, nanobelts, nanosprings, nanoring, nanohelices, and nanobows that can be obtained by the variability of surface charges and chemical compositions at the polar surfaces of the wurtzite nanocrystal structure [41, 48]. The non-symmetric wurtzite shape of ZnO is made up of alternating tetrahedrally coordinated O^{2-} and Zn^{2+} ions, arranged along the c-axis $(01\bar{1}0)$ (Figure 3) [16]. The ZnO nanostructure is also characterized by spontaneous polarization along the c-axis, despite the normal dipolar movement that is caused by the positively charged ions of Zn^{2+} (0001) and negatively charged O^{2-} $(000\bar{1})$ at the polar surfaces [41]. ZnO crystals can be formed via the hydrolysis (Eqs. (1)–(5)) of Zn salt in basic solution, to get a colorless compound, due to the $3d^{10}$ electron configuration that has zero crystal field stabilization

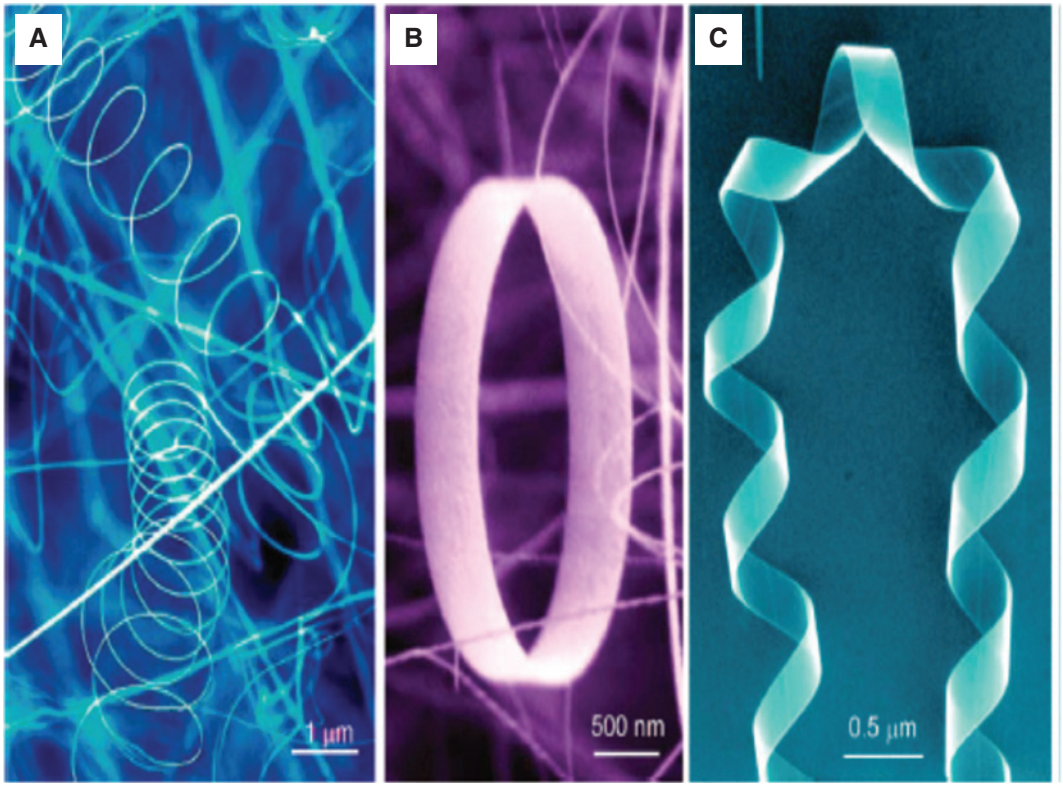

Figure 4: Examples of some ZnO nanostructures formed in nanofabrication process. (A) Nanobelt; (B) nanospring; (C) nanohelix (Reprinted with permission from Ref. [41], (A) copyright 2004 by Elsevier Ltd; (B) copyright 2004 by the American Association for the Advancement of Science; (C); copyright 2007 by Cambridge University Press).

energy [16]. Hence, the adsorption of the monolayers of the precursor molecules on the polar surfaces transforms the polar surfaces into inverted polarity. Generally, KOH is preferred to NaOH for the hydrolysis because K^+ has a larger ionic radius, which lowers the probability of fusing to the ZnO lattice [49].

$$Zn^{2+} + 2OH^- \leftrightarrow Zn(OH)_2 \quad (1)$$

$$Zn(OH)_2 + 2OH^- \leftrightarrow [Zn(OH)_4]^{2-} \quad (2)$$

$$[Zn(OH)_4]^{2-} \leftrightarrow ZnO_2^{2-} + 2H_2O \quad (3)$$

$$ZnO_2^{2-} + H_2O \leftrightarrow ZnO + 2OH^- \quad (4)$$

$$ZnO + OH^- \leftrightarrow ZnOOH^- \quad (5)$$

The growth of ZnO is generally influenced by the concentration of $Zn(OH)_2$ and the pH of the solution [16, 50, 51]. In the initial stage of the formation of ZnO, the Zn^{2+} and OH^- ions in Eq. (1) undergoes dehydration via a proton transfer that results in the formation of $Zn^{2+} \cdots O^{2-} \cdots Zn^{2+}$ bonding, which agglomerates to an octahedral shape $[Zn_x(OH)_y]^{(2x-y)-}$ [16, 52]. Research has shown that the $[Zn_x(OH)_y]^{(2x-y)-}$ aggregates formed in Eq. (2) are initially with < 50 ions, but the introduction of the O^{2-} brings about an increase in the ions to about 150 with a resultant formation of wurtzite [16], which increases in size with a core of approximately 1 nm at an ion count of over 200 [52]. Again, the formation of the ZnO nuclei according to the steps shown in Eqs. (1) to (5) is slow and can be the controlling step for the ZnO film formation that results in the growth along the basal plane, due to the relatively high surface energy [50].

Minimization of the total energy contributed by spontaneous polarization and elasticity at the polar facets, due to the spontaneous polarization across the nanobelt thickness, may result in the formation of nanospring that forms, due to the rolling of a single-crystal nanobelt [41]. When the nanospring is folded circularly as the opposite sides of the polar surface meet face to face, a nanoring will be formed, whereas the formation of nanohelix is caused by the chemical bonding of crystal stripes of nanobelts, due to the alternating and periodical distribution of the crystal strips, twisting and coiling along the growth direction (see Figure 4) [41].

Growing ZnO using pulsed laser ablation with Zn target in water, ammonia nitrate, and cetyltrimethylammonium bromide (CTAB) at temperatures of 45°C, 65°C, and 85°C resulted in morphology variation from spherical to nanoflakes, nanosquares, and branched nanorods [53]. It was also observed that the increased absorbance of ZnO was possible, due to the increase in laser fluence when it was grown in water. There was also increased nanoparticle concentration with the increasing of the fluence with the higher absorption of the spectra of the ZnO resulting in the higher band gap and the smaller the size of the nanoparticle [53] (Figure 5). On the other hand, ZnO nanoparticles prepared in 0.01-M ammonium nitrate in the pulsed laser ablation produced a rod-like wurtzite with hexagonal shape and cubic zincite ZnO phase [16, 31].

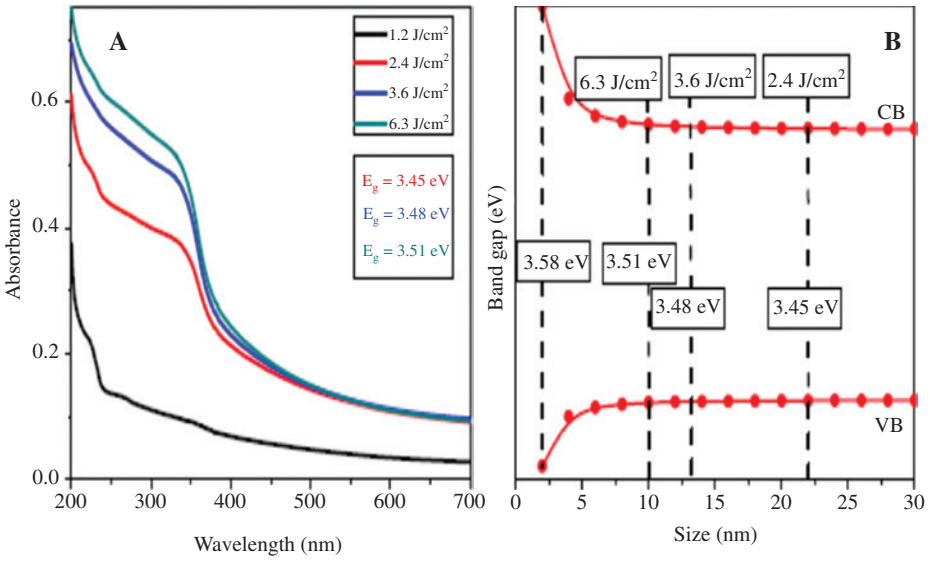

Figure 5: Variation of ZnO spectra absorbance with laser fluence wavelength and the effects of the band gaps on nanoparticle sizes. (A) Absorption spectra of ZnO obtained from laser ablation in deionized water at laser fluence 1.2, 2.4, 3.6, 6.3 J/cm². (B) Band gap variation with size of ZnO nanoparticles (Reprinted with permission from Ref. [53], copyright 2017 by Elsevier).

2.3 Characteristics of molybdenum disulfide (MoS_2)

The use of solution-based 2-D MoS_2 nanosheets for directional epitaxial growth of some noble metals such as Pd, Pt, and Ag nanostructures at room temperature has been achieved with a distinguishable (111) and (101) structural orientation on MoS_2 (001) surface [14]. This nanosheet-templated epitaxial growth was achieved via a wet chemical reaction of the nanostructures that had the MoS_2 nanosheets providing the nucleation sites for the growth of the noble metals and prevented the aggregation of the nanoparticles. This epitaxial growth phenomenon had involved *in situ* synthesis of the noble metals on the surface of the MoS_2 in a photochemical reduction technique that involved the use of CTAB at some instances.

Importantly, CTAB, which works as an orientation surfactant in nanofabrication, has various nanostructure orientations at different concentrations of the substrates and other experimental conditions [53] with increased concentrations resulting in higher epitaxial growth due to the CTAB-micelle, which bond to the substrate ions [53, 54]. MoS_2 has synergistic effects on the anode of lithium-ion batteries, a characteristic that will makes it possible to ascend battery capacity upon recharge, due to the oxidation of MoS_2 to MoS_3 [55]. Again, with MoS_2 nanosheets showing a slight decrease in specific capacitance of 14.9% in 500 cycles, it will make an excellent electrode material for electrochemical capacitors [56].

2.4 Characteristics of graphene oxide (GO)

Graphene has a 0 ev band gap because of the empty valence band that touched the conductance band that also has no valency electrons, a characteristic that gave rise to the peculiarities of graphene oxide nanostructures [57–59], hence, the application of graphene oxide nanosheets in many electronics and catalytic energy storage devices [60, 61]. The presence of the lattice of equivalent sublattices of carbon atoms that are sigma (σ) bonded with each other in a π orbital altered the electronic configuration of the material [62]. Graphene oxide-based templates help in the formation of the hexagonal structure Au nanosheets by the absorption of amine molecules [60] and for the assembly of Au nanodot chains using long-chain thiol molecules of the reduced graphene oxide [61]. Similarly, pyrolytic graphite substrates used in nanofabrication guaranteed better fusion of thiol-capped nanoparticles such as Ag into the epitaxial geometrical orientation, due to the limited defects on the structure [63].

3 Nanostructures fabrication techniques

Nanostructures have been fabricated with a top-down approach that involved the use of lithographic etching of materials, for shaping and patterning the orientation of nanostructures, whereas the bottom-up technique involves the growing of nanostructures with atomic-scale systems that utilizes adatoms for deposition of vaporized materials on substrates and templates [3, 16]. There are different bottom-up fabrication approaches such as the wet chemical method [14, 16], physical vapor deposition [64, 65], metal organic chemical deposition [66, 67], molecular beam epitaxy [68], pulsed laser deposition [69], sputtering [70], flux method [16], and electrospinning [71] used for the fabrication of nanostructures. Some of the major characteristics of these fabrication techniques include controllability of fabrication conditions such as temperature, pressure and deposition rate, uniformity of nanostructure, high-quality nanomaterial with limited impurities, reproducibility that will enable the scale-up of the process into commercial production, high throughput, choice of substrate and template material for fabrication, and excessive cost of fabrication [15, 16]. A summary of some of the bottom-up and top-down fabrication techniques is shown in Table 1.

3.1 Fabrication concepts and attributes of nanostructures

Nanotubular structures attain better anti-reflection than nanoparticles or deposited materials due to the high porosity that can be up to 70% [81]. A nanoporous polyimide template prepared by dry etching using anodized alumina oxide membrane mask, followed by atomic layer deposition of alumina, was used for fabricating the high-density, free-standing alumina nanotube arrays [81]. The variation of the pore size, thickness of the nanoporous polyimide template, and deposition thickness of alumina, helped to obtain nanotubes with various diameters, lengths, and wall thicknesses. Similarly, the optical properties of these alumina nanotube arrays, modified by changing the wall thicknesses on glass, showed an anti-reflectance with a 0.1% reflectance at the visible wavelength of 540 nm. The broadband and omnidirectional

Table 1: Summary of the characteristic of some nanostructure fabrication techniques.

Lithographic method
- Uses electron beams to remove micro-scale structures from resists, which are precursor materials
- Can fabricate nanostructures of ~45 nm
- Transfers a mask image to a substrate by coating while exposing the resist to electron beams and applying appropriate chemicals to develop the image on the substrate
- The technique uses physical masking that involves the resist surface being in contact or in proximity with the mask or by software mask, which uses computer programs for patterning the mask
- The cost of using this technique is high, as equipment could cost from hundreds of thousands of dollars to millions of dollars [72]

Pulsed laser deposition
- Involves physical vapor deposition of thin films using high-powered beam to strike a deposition material in a vacuum chamber
- The technique can also work in the presence of oxygen when depositing complex oxides
- It can work at a temperature that varies from room temperature to above 1000°C
- Temperature, laser energy density, pulse repetition rate, pressure, type of gas inside the chamber, and substrate-to-target distance determine the quality of the nanostructures produced
- There is no uniformity of produced nanostructures, due to the narrow forward angular distribution of the plasma plume [16, 73]

Electrodeposition
- Uses induced electrochemical reaction in aqueous solution to deposit nanomaterials on metal oxides and chalcogenides
- Growth of electrodeposited materials is outward on the substrate and can be controlled by using an insulating mask
- It is a cheap nanofabrication process that can be done at room temperature using water-based electrolytes
- Controlling of charging rate and time can be used to monitor the rate of deposition of films on the substrate, which can range from a few nanometers to tens of microns
- The technique has been exploited for the nanofabrication of complex 3-D materials such as the interconnections in computer chips
- The nanofabrication can be scaled-up from an atom deposition to large-scale dimension [74, 75]

Metal organic chemical deposition
- Relies on the transfer of materials in gas phases for deposition on substrate surface through a chemical reaction
- The temperature for the nanostructure fabrication is in the range of 500°C to 1500°C, and the sample can be rotated at 1500 rpm to maintain the uniformity and quality of the produced nanocrystals
- The fabrication can be done at near atmospheric pressure
- There is a limitation on the choice of substrate needed for the fabrication [16]

Wet chemical method
- Temperature and other parameters that control the morphology of the nanostructure can be controlled during the fabrication process, to enhance the characteristics of the nanostructures
- The fabrication can be done at low temperature using flexible organic substrates that may not require catalysts
- The technique can be used with silicon technology, which has found many applications in semiconductors [14, 16]

Physical vapor deposition
- Requires elevated temperature deposition of sublimed source material
- Can incorporate impurities to nanostructures from the reactor chamber or from the use of catalysts in the nanofabrication
- May not be integrated with flexible organic substrate; however, as a self-assembly technique, it requires a material to be deposited on substrates
- Temperature, pressure, and carrier gas control the catalyzed process of physical vapor deposition [16, 76]

Flux method
- This technique fabricates nanostructures at elevated temperature and can incorporate impurities to the nanostructure
- As a bulk crystal growth phenomenon, reactants are dissolved at elevated temperatures in molten salt to form complex materials
- Controlling and altering the concentration of the molten complex compound and the temperature of the reaction helps to obtain a 1-D nanotube and other nanostructures
- Alkaline hydroxides are the widely used flux for synthesis of oxide nanostructures due to their low melting points [16, 77, 78]

Molecular beam epitaxy
- Provides a single crystal film of heated substrate under high ultralight vacuum condition
- Can fabricate single atomic crystalline layers at a time with the possibility of controlling the morphology of the nanostructure in the growth process
- The fabricated nanostructure may have a uniform morphology and high quality with reduced impurity
- Performance of the devices fabricated by this technique depends on the dopant control and the hyper-abrupt interfaces of the crystalline film layer
- Can be used to fabricate nanostructures of different geometries from 1-D to 3-D
- The limited choice of substrates may have to contribute to the poor yield of nanostructures produced by this technique, which is not cost effective [16, 68]

Table 1 (continued)

Electrospinning
– Used for generating nanofibers from materials such as polymers, composites, and ceramics
– Consists mainly of a high voltage supply, a spinneret, and an electrically conductive collector
– Controlling of the humidity, temperature, and pressure is vital for nanofiber fabrication using ceramics
– The electrospinning process helps to generate continuous charges on the surface of liquid droplets used for the nanostructure fabrication [79]
Sputtering
– The technique is scalable for mass production and works at low pressure in a reactor chamber that contains inert gas such as argon
– Electromagnetic signals in the reactor turns the inert gas into plasma and accelerate the positive ions toward the substrate with a kinetic energy of ~10 eV
– The sputtered atoms pass through the plasma and deposit on the substrate causing growth of nanocrystals that may be influenced by the collision of the sputtered ions with heavy particles in the plasma, resulting in loss of energy, direction, and not depositing on substrate
– Film morphology may be altered by the high kinetic energy of sputtered particles due to the atomic mobilization process [80]

anti-reflective characteristics of a passivated conical frustum array of 550-nm height, fabricated with polystyrene colloidal lithography on a crystalline silicon nitride of 80-nm thickness, caused the suppression of the Fresnel reflection at a visible wavelength (400–1000 nm) at an incident angle of ~60° [82]. Tseng et al. [82] also showed that the power conversion efficiency of 13.39%, which is 9.13% enhancement from the conventional KOH-textured silicon cell, was achieved, while the measurement of the external quantum efficiency showed that photocurrent was driven primarily by the increased optical absorption in near infrared.

α-Fe_2O_3 can make a potential anodic material for lithium-ion batteries because of the low cost, environmental friendliness, corrosion-resistive qualities, and high thermal capacity of ~1007 $mAhg^{-1}$ [4, 28, 83]. The fabrication of the hollow-structured α-Fe_2O_3 nanofibers was done using the electrospinning technique with iron acetylacetonate ($Fe(aCaC_3)$) and polyvinyl pyrrolidine (PVP) used as precursors [4]. The calcination of ($Fe(aCaC_3)$)-PVP composite fiber at a high temperature helped to form the interconnected 1-D hollow structure of the α-Fe_2O_3 nanofiber that exhibited a reversible capacity of 1293 $mAhg^{-1}$ at a current density of 60 mAg^{-1} at the anode. This material also displayed an excellent cycle stability and rate capacity at a large aspect ratio, which makes it a suitable material for lithium-ion batteries.

To overcome the charge transport limitation that is peculiar with conventional nanoparticle-based photoanodes [84, 85], tin-doped indium oxide nanowires were used to prepare the dye-sensitive solar cell photoanodes, by vertically growing tin-doped indium oxide nanowires, using the thermal evaporation process. The TiO_2 shell layer was also utilized to uniformly coat the nanowire surface to ensure a high dye loading [5]. These researchers [5] reported that the cell efficiency increased to 4.85% from the 2.81% obtained when a dense HfO_2 blocking layer was inserted between the tin-doped indium oxide nanowire surface and the porous TiO_2 shell layer. This increase was attributed to electron recombination, which was achieved at a nanowire length of 20 μm. Moreover, the decrease in the TiO_2 annealing temperature, from 600°C to 400°C, resulted in an increase in electron recombination, due to the higher dye loading on the TiO_2 nanoparticles, resulting in an efficiency of 5.59% of the photoanodes.

The block copolymer has stood out as a lithographic template, separation membrane, and organic photovoltaic layer due to the self-assembly attributes, which makes it possible for nanofabrication [86]. Different annealing techniques such as thermal, solvent vapor, magnet, and electrical field alignment have been used to self-assemble block copolymers, whereas *in situ* X-ray and neuron scattering have been used for studying the thin film of the block copolymer, annealed with different protocols [86]. Controlling the morphology, ordering, and orientation of the block copolymers using X-ray and neuron scattering has the potentials of linking the thermodynamic pathway of the nanostructures' growth mechanism over the macroscopic areas, during nanofabrication [87]. The use of X-ray and neuron scattering can also help to refine annealing techniques for block copolymer, foster robust fabrication procedures, while helping to develop the next generation of direct block copolymer assembly of nanostructures using hybrid systems that can combine top-down and bottom-up fabrications [88].

To fabricate hierarchical 3-D branched TiO_2/Si nanowire arrays, some researchers [89] combined nanoimprint lithography and reactive ion etching process, while using a high-resolution scanning electron microscope for examining the morphology of the nanostructures. They also used X-ray diffraction for studying the crystalline structures of the TiO_2 nanowires, which were hydrodynamically grown

on the Si substrate. The work of Noh et al. [89] revealed that the increased surface area of the electrochemical reaction [28, 30, 90] and enhanced charge transfer dynamics [41] caused the improved photo-electrochemical performance of the TiO_2/Si nanowire arrays when compared with the TiO_2 thin film-coated Si nanowire arrays.

The existence of neutrality levels of surface state donor-acceptor continuum makes the characterization of surface state, based on photoluminescence and cathodoluminescence possible, hence, the ease of forming electron-collecting and hole-collecting nanocontacts for nanostructures without p-n junctions [91]. It is, therefore, important to passivate the Si interface control layers to enhance the power supply ability of the molecular beam epitaxy grown quantum wires, which have potential applications in solar cells, as an intelligent chip, in photovoltaic energy generation. Hence, after adding different atoms of metallic elements in a single-phase ternary metal chalcogenide nanowire of < 20-nm diameter, the scalable ultrathin composition of tellurium selenium-doped ternary chalcogenide nanowire was fabricated by utilizing the templates of the $Te_{1-x}Se_x$ alloys [92]. This nanomaterial was found to have a high thermoelectric figure of merit of 0.75 and a power factor of 1023 $\mu W/mK^2$, be temperature dependent, and with a setback coefficient that suggests that the charge transfer mechanism was dominated by an energy barrier between the nanowire-nanowire nanojunctions. As the energy barriers, substrates, deposition time, and physical and chemical characteristics of the chemicals and catalysts can potentially affect the characteristic, morphology, and orientation of the fabricated nanostructures [2, 9, 16, 90], it is important to understand their impacts on the nanostructures' geometry and behavior. To this end, some researchers [93] aimed to clarify the role of the Si organization on the surface orientation of the nanostructures by studying the first stage of growth of the Si on the Ag (001) surface at room temperature, using the Auger electron spectroscopy and low-energy electron diffraction. They confirmed the existence of a layer-by-layer, non-long ordered structure at about one monolayer of the nanostructure and a complex overlaying pattern that has no clear symmetry and growth pattern following.

Other researchers that worked on nanostructure fabrication such as Wu et al. [94] synthesized nitrogen-doped p-type ZnTe nanowires using chemical vapor deposition and affirmed that metal oxide-semiconductor field effect transistors have enhanced subthreshold swings and threshold voltage compared with junction field effect transistors. However, the junction field effect transistors have higher transconductance and I_{on}/I_{off} ratio than metal oxide-semiconductor field effect transistors. On the other hand, the wet chemical synthesis fabrication of the Pt-MoS_2 hybrid nanostructure resulted in a higher electro-catalytic activity of the material toward the hydrogen evolution reaction compared to the commercial catalysts made with the same platinum (Pt) loading [14]. Similarly, the use of pulsed laser atomic probe tomography for analyzing dopants and other impurities in Si and Ge nanowires fabricated with vapor liquid solid mechanism was used by other authors [95] to determine the concentrations of phosphorous in silicon (Si) nanowires and boron (B) in germanium (Ge) nanowires. However, impurities associated with nanostructures used for developing semiconductors have the potentialities of showing homoepitaxy of atom-like structures and coherent attributes that may be vital for future applications in optical quantum computing and communication networks [96].

4 Growth mechanisms of nanostructures

The growth of nanostructures during fabrication depends on different conditions that can affect the structural growth along a given direction and results in different growth morphologies and characteristics [30]. The growth direction can depend on the surface energy, which tends to direct growth more, along the facets with higher energy (because of their smaller surface areas) to the detriment of surfaces with lower energy [16, 30, 41]. This situation is evidence in the anisotropic growth of ZnO nanostructure that is highest along the c-axis at the facets $\{01\bar{1}0\}$ and $\{2\bar{1}\,\bar{1}0\}$ with growth directions of-$(2\bar{1}\bar{1}0)$ ($\pm[2\bar{1}\,\bar{1}0]$, $\pm[\bar{1}2\bar{1}0]$, $\pm[\bar{1}\,\bar{1}20]$); $(01\bar{1}0)$ ($\pm[01\bar{1}0]$, $\pm[1\bar{1}00]$), and $\pm[0001]$ [32]. Other researchers also demonstrated the structural specificity of nanostructures on colloidal synthesis using a method that spontaneously resulted in facet selective growth of ZnO nanorods, on the {111}, rather than on the {100}, facet of Ag nanocrystals [97]. The heterogeneity of the nanostructures in this experiment that was performed by Fan et al. [97] using seed-mediated method of growing ZnO nanorods on Ag-truncated nanocube surface was confirmed with select-area electron diffraction and convergent-beam electron diffraction. The results indicate that the ZnO nanorod grew along $\{01\bar{1}0\}$ and the Ag nanoparticles grew along $\{\bar{1}12\}$ with an epitaxial relationship as $[01\bar{1}0]_{ZnO}||[\bar{1}12]_{Ag}$ and $(0002)_{Zn}||(111)_{Ag}$ [97]. Again, Piñero et al. [98] fabricated nanowires by growing on the [111] facet of the Si-oriented substrate, GaAs crystals using the molecular beam epitaxy and vapor-liquid-solid fabrication process. They discovered that the nanowires were mainly growing

in alternative wurtzite and zinc-blended phases, a result that can be attributed to the enhanced attractive interaction of the facet, which was caused by lattice mismatch of the GaAs on the Si substrate. It is noteworthy that lattice mismatch prevents nucleation and growth of over-layer on substrates, due to the existence of structural strains [99–101]. Furthermore, another research that involved the growth of noble metal-Pt on a single-layer MoS_2 nanosheet at room temperature, using wet chemical synthesis, produced two epitaxial orientation, [111] and [101], that coexisted for the metal nanoparticles [14]. Huang et al. [14] also affirmed that the anisotropic nanostructure of the Pt epitaxially aligned on the MoS_2 nanosheets with the [111] and [202] spots being aligned with the [100] and [110] diffraction spots of MoS_2, respectively.

4.1 Factors affecting nanostructure growth and characteristics

Nanostructure growth is affected by numerous variables, which have been summarized in Table 2.

4.2 Growth mode of nanocrystals

The growth of ultrathin films of nanostructures and nanocrystals is fundamental to achieving the expected morphology, size, orientation, uniformity of growth, and other characteristics of the fabricated nanostructures. Generally, the growth mode of nanocrystals and nanostructures involves an orientation attachment

Table 2: Summary of some factors affecting the growth rate of nanostructures.

Factor	Impacts/remarks	Ref
Diffusion	– Growth rate is determined by diffusion rate	[102–106]
	– Nucleation of nanoparticles is influenced by electrical strain, surface energy, and surface diffusion kinetic	
	– Liquid phase enhances the growth in vapor-liquid-solid mechanism	
	– Nanowires with smaller diameters grow faster than those with bigger diameters for systems having limited-mass-transport growth mechanism else the reverse is the case due to Gibbs-Thomson effect	
	– Diffusion of adatoms of nanoparticles on the sidewalls of the nanowire causes smaller diameter nanowires to grow faster than those of bigger diameters	
Buffer layers and catalysts	– Buffer layers' result in varying morphology due to the different growth rates	
	– Buffer layers can act as a seed layer to enhance the coverage and growth rate of the nanostructures	
	– Catalysts facilitate the growth rate via increased collision and nucleation	
	– Catalysts initiate and guide growth and epitaxial orientation between the nanostructures and the substrates	
	– Introduction of polydopamine on carbon fiber increased adhesive strength between carbon fiber and ZnO nanowires and the interfacial shear strength	
	– Impurities from catalysts can change the characteristic, size, and orientation of nanostructures	
	– Quantity of catalyst and particle flux affect the growth of nanowires	[41, 107–113]
Temperature	– Nanowire diameters increase with increased growth temperature	
	– 1-D ZnS nanocrystals were obtained at low density and high temperature (1000–1100°C) and nanowires were obtained in low temperature (800–1000°C) for a thermal evaporation nanofabrication technique	[8, 114]
Surface energy	– Area of high surface energy enhances nucleation and formation of colonies of nanoparticle and facilitates nanocrystal formation	[13, 28]
	– High aspect ratio of nanostructures favors higher surface area for chemical reaction	
Orientation	– Si nanowires prefer to grow along the [112] orientation, followed by [110], [111], [001], [113], and [133]	[13, 115–120]
	– Growth orientation is determined at precipitation	
	– Surface chemistry of substrates and reaction pressure determine orientation of nanostructures	
	– Nanowire diameter and precursor molar ratio impact the orientation of nanostructures	
	– Chemical composition of initially allowed droplets influences orientation of nanostructures	
Doping and alloying	– Doping and alloying are used to influence the physical properties such as electrical conductivity, band gap, and ferromagnetism of nanostructures	[41, 121, 122]
	– Temperature and doping affect the nanocrystal size	
	– N-type, p-type, and transition metal doping techniques have been used to influence the characteristics of nanostructures	

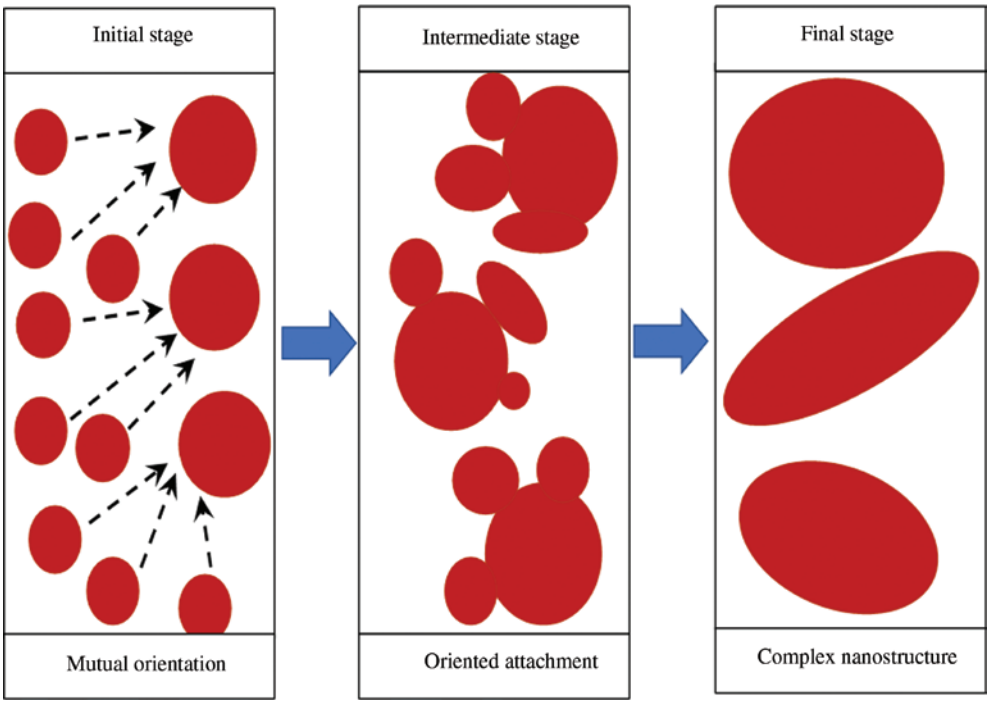

Figure 6: Nanocrystal orientation-based growth mechanism due to Oswald's ripening of poly-dispersed nanocrystals.

mechanism, crystallization process, and particle-based aggregation [123].

4.2.1 Orientation-based attachment growth

Poly-dispersed nanocrystals can be influenced by Oswald's ripening, which is a procedure by which larger-sized nanocrystals grow at the expense of the smaller size ones because the chemical potential difference between them triggers diffusion that causes the loss of the mass of the smaller particles to the larger particles [124]. This orientation-based attachment growth can involve the attachment of smaller particles together in the growth process by sharing crystallographic orientation and docking at different planar interfaces [125] due to the energy difference in the particles, which make larger particles grow more than the smaller ones. Oriented-based attachment also causes a reduction in the high-energy surfaces and the reduction of surface free energy that plays a significant role in the particle integration process [126]. Orientation-based attachment growth is dependent on the effective collision of particles, and the number of collisions in each surface area determines the level of mutual orientation attachment growth, in a well-dispersed colloidal suspension (Figure 6) [126]. This collision of particles is expected to result in a statistical growth process, whereas coalescence induced by particle rotation, which is dominant in a weakly flocculated colloidal state, leads to the formation of complex structures after the orientation-based growth [126]. As Oswald's ripening process is continuous in a poly-dispersed medium, destabilization and sedimentation could follow [127]; hence, it is important to stabilize dispersions to avoid coarsening [128].

4.2.2 Nucleation process

Nucleation, which is the build-up of molecule clusters before the formation of new phases in the transformation of vapor to liquid to solid, is characterized by the decrease in enthalpy and entropy of the system after surmounting the free energy barrier per Eq. (6) [125]. The random collision and rearrangement of atoms and molecules at a given phase of transformation, and the growth of the nanoparticles in clusters, which can be a reversible and stepwise kinetic process, contribute to the nucleation process [125]. The critical size of the nucleus ($r^* = 2$–3 nm nanoparticle) is essential for the nucleation process and formation of clusters per Figure 7.

$$\Delta G = \Delta H - T\Delta S > 0 \tag{6}$$

where ΔG is the change in Gibb's free energy, ΔH is the change in enthalpy, T is the temperature, and ΔS is the

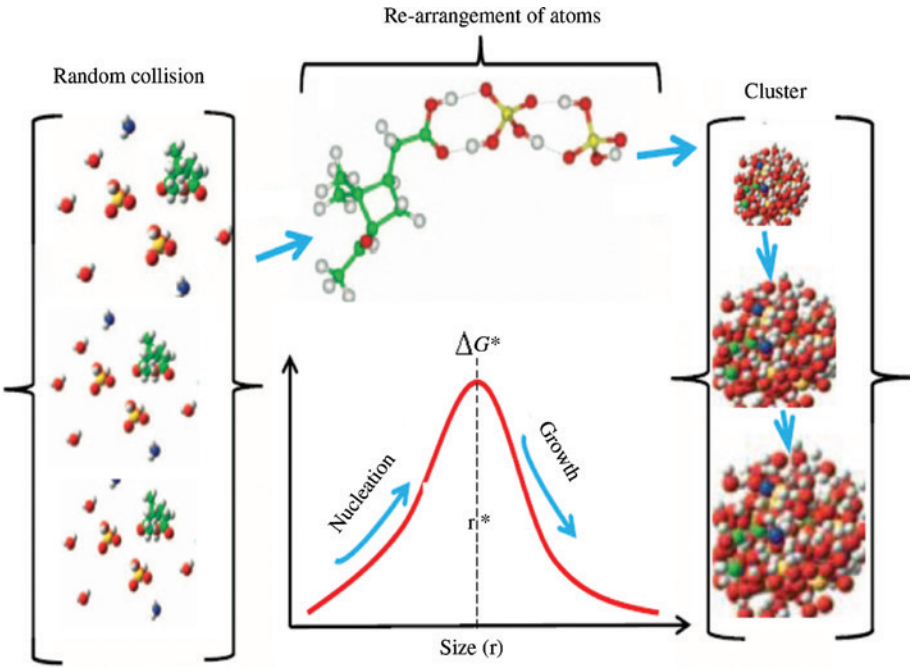

Figure 7: Nucleation and cluster formation of nanocrystals showing the random collisions, re-arrangement of atoms, and clustering.

change in entropy. ΔG^* is the change in Gibbs free energy at the critical radius.

At the critical size of clustering of the nucleus, growth becomes spontaneous, despite the ease of dissociation of the clusters due to the very slow short life span. However, a few of the clusters get to the critical size and continuously grow spontaneously to form larger particles [125]. This growth is governed by thermodynamic principles, which is controlled by the chemical potential difference that is related to the pressure in the system at equilibrium per Eq. (7) [129, 130].

$$\Delta\mu = \mu_v - \mu_s = RT\ln\left(\frac{P}{P_0}\right) \tag{7}$$

where $\Delta\mu$ is the thermodynamic driving force, μ_v is the chemical potential of the vapor, μ_s is the chemical potential of the substrate, P is the partial pressure at the gas phase, and P_0 is the equilibrium partial pressure of the components over the nanocrystal at a given growth condition.

Nanowire growth is also affected by the wetting angle, surface polarity, surface energy, and chemical activities at the crystalline planes [31, 131]. At the crystalline planes, the surface energy and the catalyst-vapor triple-phase boundaries are important in growth facilitation because the thermodynamic driving force ($\Delta\mu$) of the nanocrystals can vary with the wetting angles [131]. Hence, for growth to take place, the nanocrystals must surmount the free energy (ΔG) barrier in the nucleation process [125] and form clusters. The free energy at the catalyst-nanowire interface (ΔG^{cni}) can only form the nanoparticle layer necessary for homo- and heteroepitaxy when the conditions in Eq. (8) are met [131].

$$\Delta G^{cni} = \alpha N^{0.5} - \Delta\mu N \tag{8}$$

where α is a geometrical weight coefficient for forming a new surface from the cluster of adatoms (N).

Generally, the nucleation in the nanofabrication process is expected to take place when the thermal activation energy (ΔG_B) is reached, and the critical nucleation (J_C) can take place in an environment that depends on the temperature (T) and concentration of monomer (C) per Eq. (9) [131].

$$\begin{cases} \Delta G_B = \dfrac{\alpha^2}{4\Delta\mu} \\ J_C = ZC\omega\exp\left(\dfrac{-\Delta G_B}{K_bT}\right) \end{cases} \tag{9}$$

where K_b is the Boltzmann's constant, and Z is the Zeldovich factors.

During the nucleation process, phase transition is vital for the estimation of the size and number of nuclei that is formed [130], and the nucleation rate (I_n) for a

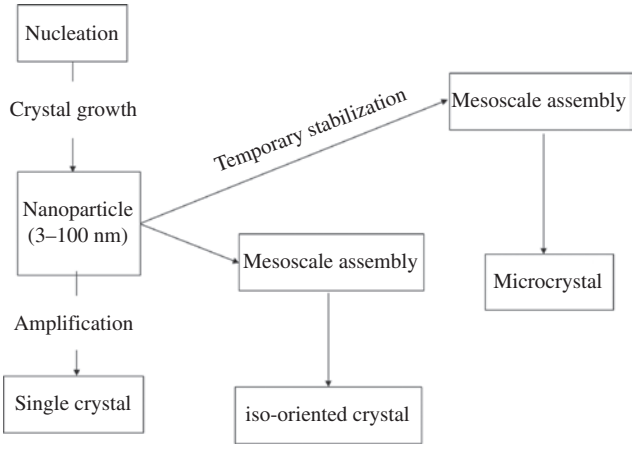

Figure 8: Schematic of aggregation-based nanoparticle crystalline growth.

multicomponent nanomaterial can be estimated with Eq. (10) [130].

$$I_n = n_l\left(\left(\sum_{k=1}^{m}\omega_k\right)\exp(H_0)\right) \tag{10}$$

where ω_k is the diffusion coefficient of the *kth* component of a nanomaterial of the *m*-components, H_0 is a barrier to the multicomponent, and n_l is the initial phase density of the molecules.

4.2.3 Classical crystal growth mode

This process occurs by the atom to atom addition to a template or by the dissolution of unstable phases and precipitation of more stable phases. This phase is critical to the nanostructure fabrication because the parametric control of the process of adatom growth influences the characteristics, orientation, and geometry of the nanostructures [16, 30]. The precipitation and formation of the nanocrystals is preceded by nucleation that occurs by the dissolution of the nanoparticles at a high temperature and cooling to a lower temperature [123] and by the addition of a necessary reactant to produce a supersaturation state.

4.2.4 Aggregation of particles

In this state of the nanocrystal growth, particles grow by aggregation in a mesoscopic transformation process that allows them to increase to a stable size and then start combining with unstable particles until the formation of a single nanocrystal structure. The nanoparticles can also grow into iso-oriented crystals via orientated attachment after fusion and can also form a mesoscale assemble with the formation of microcrystals [123]. The schematic of the aggregate-based nanoparticle crystalline growth is shown in Figure 8.

4.3 Heteroepitaxy of nanostructures

In the growth of nanostructures, there is a tendency of order and disorder in the heteroepitaxy of structures due to a small lattice mismatch of layers on the template or substrate [132]. This disorder usually stalls the improvement in the physical properties of the nanostructures that can be achieved via fabricating a uniform size, proper shape, and regularly positioned nanostructures. Hence, there is the need for control of the different parameters such as temperature, deposition time, pressure, and chemical concentrations of precursors during the nanofabrication process [13]. The nanostructure fabrication process can result in the growth of 3-D interfaces due to the strain mechanism on the substrates and the templates, which results in the formation of Volmer-Weber growth mode – the formation of 3-D islands directly on bare substrates – and the Straski-krastanov growth mode – the formation of an initial flat wetting layer on substrates and templates [132]. As these growth modes can result in heteroepitaxy and quantum dots in 3-D nanostructures, experts are still working on techniques to harness the advantages of heteroepitaxy in novel industrial applications [132]. Although heteroepitaxy, which is also attributed, in part, by differentiation in thermal expansion and lattice mismatch of materials used for nanofabrication [18, 132], could have potential future applications in the industry, however, the strains induced on the nanostructures by heteroepitaxy have resulted in defects and microcracks at the interfaces, with performance efficiency reduction for charge-transferring devices [18]. A high deposition temperature, which make deposited adatoms on substrate surfaces to diffuse easily on the substrates have also hampered homoepitaxy in favor of heteroepitaxial growth of nanostructures [133].

Mitigating against the influence of heteroepitaxy will be vital for the reduction in the level of uncertainties associated with nanostructure characteristic flaws, hence, the need for buffer layers in planar structures, to aid the reduction of lattice mismatch and thermal expansion strains during nanofabrication [133–136]. Again, the improvement of the interfacial qualities of the nanostructures via reduction of the footprints of crystals in growing thin-film nanostructures will also help to improve the

nanocrystal qualities, due to the reduction of the strains on the sidewalls of nanotubes [18].

5 Growth models of anisotropic nanostructures

Physical, statistical, physical-statistical, and cross-domain models have been predominantly adopted for modeling the growth process of nanowires, due to the limited data availability and the complexities associated with the growth process of this nanostructure [136]. Statistically, different approaches have been adopted for predicting the process conditions affecting the morphology of nanowires based on the observed and unobserved variables that can be predicted using prior conditions of the system. Different statistical techniques such as fractional factorial design, multinomial regression models, Gaussian Markov random field, bivariate Gaussian distribution, and box-Behnken design have been adopted by numerous researchers [136–140].

The growth of nanowires was described with a diffusion-induced phenomenon, with stationary equations that depended on the decreasing radius of the nanowire (R) in the form of $1/R^p$, where p has a value of 0.5–2 and depended on growth conditions [141]. Size-dependent, non-linear effects in nanowire growth of crystal structures, kinetics and nucleation statistics in individual nanostructure layers, length of distribution of nanowires, radius of growth rate under varying conditions, number of growth islands, nucleation time, diffusion constants, and diffusion rates [141–145] are among the conditions that determine the diffusion-induced growth rate of nanowires. The approximate normalized diffusion flux of adatoms via a circular triple phase line at the nanowire top (Z = L) for a time-dependent nanowire growth $\left(\left(\frac{dL}{dt}\right)_{\text{diff}}\right)$ with radius R is shown in Eq. (11).

$$\left(\frac{dL}{dt}\right)_{\text{diff}} = -\frac{2\Omega_s}{R} D_f \left.\frac{d_{n_f}}{dz}\right|_{Z-L} \tag{11}$$

where L, Ω_s, D_f, n_f, and Z represent nanowire length, elementary volume in the solid, diffusion coefficient, the z-dependent adatom concentration on the sidewall facets, and vertical coordinate, respectively.

The growth kinetics of a graphene nanostructure fabricated with chemical vapor deposition was determined with a stochastic mathematical framework with a generalized equation for growth velocity $V_i(\theta,t)$ at a given shape of graphene island $g_i(\theta)$ and growth-driving forces $q(t)$ at a given time t shown in Eq. (12) [144].

$$V_i(\theta,\ t) = g_i(t)q(t) \tag{12}$$

The model in Eq. (12) is linked to measurable variables in the graphene nanostructure over a given polar space, by considering the growth radius, area of growth, and nucleation time. The driving force of the nanostructure growth over a given time has been associated with the shaded area of the graphene nanoparticle growth $s(t)$ and the number of graphene islands (N_t) at time t per Eq. (13) [146].

$$q(t) = \frac{ds(t)}{dt} / 2\sqrt{N_t s(t)} \tag{13}$$

By assuming a constrained birth process that has the time of growth of the graphene nanoparticles as a Poisson process, which functions as a non-homogenous intensity function, the growth-driving force at time t was modeled per Eq. (14) [144].

$$q(t) = \frac{\left\{\frac{1}{3} + \sqrt{\frac{17}{72}}\right\}\sqrt{[\alpha^3[1-e^{-\alpha\omega}]]}e^{-\alpha t}}{\sqrt{[A_{nuc}\beta\{1-e^{-\alpha t}\}]}} \tag{14}$$

where A_{nuc} represents the area of graphene nanoparticle island, β represents the coefficient of unnormalized shape of the graphene nanoparticle island, $\alpha > 0$ represents the parameter governing the growth on the tray, and $\omega > 0$ represents the parameter governing the relationship between α and the coverage on the tray.

As noted from Eq. (14), the increase in driving force of the growth kinetic is caused by the reduction in the graphene nanoparticle island, whereas the increase in the coefficient of the unnormalized shape of the graphene nanoparticle island leads to a decrease in the growth driving kinetic over a given fixed area.

In a vapor-liquid-solid fabrication mechanism, the physical growth rate $\left(\frac{dL}{dt}\right)$ of nanowires can be attributed to discrete deposition or diffusion as shown in Eq. (15) [147].

$$\frac{dL}{dt} = \begin{cases} \dfrac{2\Omega L(N_\infty - N_0)}{\tau R} & L \le L_f \\ \dfrac{2\Omega L_f(J - (N_0/\tau))}{R} & L > L_f \end{cases} \tag{15}$$

where τ, Ω, J, R, N_0, N_∞, L_f, D represent the mean lifetime of the adatom on a nanowire sidewall, atomic volume of

Si, impingement flux, radius of nanowire, adatom concentration at liquid alloy, adatom concentration at base substrate, diffusion length ($\sqrt{2D\tau}$), and diffusion coefficient, respectively.

An absorption-induced and diffusion-induced model of nanowire growth is shown in Eq. (16) [148].

$$\frac{dL}{dt} = V_0\left[\left(1+\frac{R_1}{Rcosh(\lambda)}\right)(\varnothing+1) - \left(1+\frac{R_2}{R}\tanh(\lambda)\right)(\varepsilon+1)\left(\frac{1}{V_*}\frac{dR}{dt}\right)\right](1-E)V \tag{16}$$

where ε, R, $\varnothing$, V, V_*, E, R_1 and R_2, and λ represent the supersaturation nucleation, droplet radius, supersaturation of gaseous phase, deposition rate, kinetic parameters that are related to the solid and liquid phase volume ratio, relative difference between deposition rate and growth rate on the substrate, constants used to consolidate various parameters in the diffusion-induced process, and the ratio of whisker length L to the adatom diffusion length on the side surface, respectively.

The uncertainty in the growth morphology of the nanostructures and the local variabilities in the growth kinetics resulted in the use of statistical framework to capture nanowire growth rate per Eq. (17) [138].

$$X(s,\, t) = \eta_{k-1}(s,\, t) + \phi(s) + \varepsilon \tag{17}$$

where $X(s, t)$ represents the nanowire length on substrate, $\eta(s, t)$ represents the morphology of the nanowire, $\phi(s)$ represents the local process conditions affecting the morphology of the nanowire, and ε represents the error inherent in the system.

The mass continuity of the diffusion length of the adatoms in the modeling of the vertical growth of nanowires with the aim of optimizing the spatial arrangement of catalyst arrays in the growth process was considered by Aghdam et al. [139]. The authors proposed the probability of the influence zone for two nanowires per Eq. (18), considering the diameters, the distance between the nanowires' radius of interaction and surface collection area.

$$P(d_{ij} < r_{\text{int}(i)} + r_{\text{int}(j)} = 1 - e^{-\delta\pi(r^2_{\text{int}(i)} - r^2_{\text{int}(j)})}) \tag{18}$$

The vertical growth (h) of the nanowire can be determined with Eq. (19) [139].

$$h_i(t+\Delta t) - h_i(t) = \Delta h_i(t) = J_p(K_s + K_w + K_d)\Delta t + \varepsilon_h \tag{19}$$

where d_{ij} is the distance between nanowires i and j, r_{int} is the radius of interaction around a nanowire, h is the nanowire height, J_p is the bulk equivalent planner growth rate, δ is the intensity parameter of Poison distribution, ε_h is the random error value, and K_s, K_w, and K_d are contribution factors from the substrate, sidewall, and droplet, respectively.

6 Application of nanostructures

Nanostructures have found numerous applications in the industry, due to the unique characteristics of the nanomaterials that have modified the characteristics of traditional materials used for different industrial purposes. Fabricated high-ratio silver nanowires have interesting applications in plasmonic devices [2], and SnO_2 nanoparticle moderated surface area have large particles for light scattering and crystallization. This makes the SnO_2 material efficient for charge transfer and, hence, have found application in dye-sensitive solar cells [149]. Similarly, quantum dots, which are nanocrystals formed from lithographic techniques such as ion beam photolithography and chemical etching [24], are very small to result in quantum confinement that can bring about discrete physical and chemical states, which are vital for developing new devices and applications [130–152].

6.1 Near-infrared (NIR) reflective and anti-corrosive function of nanostructures

NIR reflective coatings have been utilized in many industrial sectors – military, construction, plastic, and petrochemical industries, due to their ability to minimize corrosion degradation of facilities, minimize urban heat island effect, enhance the life cycle duration of facilities, enhance aesthetics, and minimize energy consumption [153]. The NIR reflective coatings with a nanomaterial blend of metal oxides such as tin and zinc have shown remarkable NIR reflectance with better color choices and quality [153].

Research has shown that paint coatings, developed from ZnO nanostructures via mechanical milling and microwave irradiation of metallic zinc dust, have high corrosion resistance because of the improvement in the oxidation kinetics, particle size distribution, morphology, phase purity, disperse and UV absorption characteristics [154]. The research showed that 33% enhancement in the NIR shielding and 156% improvement in corrosion-resistant properties (in comparison to uncoated surface) make the product have multifunctionality [154]. Again, the ZnO nanoparticle filler that were blended with cashew nut shell liquid resin as a matrix, using conventional thermal oxidation and microwave-assisted oxidation routes, also provided a high-quality coating product, due to the minimal defects in the nanostructures and morphology [155]. However, the

crystalline purity of ZnO synthesized with the microwave-assisted oxidation route showed a higher purity than that fabricated with the conventional thermal oxidation. The work of Echeverría et al. [155] also showed that the water contact angle of the ZnO nanoparticle cum cashew nut shell liquid resin-mixed coated glass was 91°, a value that is about three times higher than the water contact angle of uncoated glass that is 34°. It is important to note that a small water contact angle (<90°) enhances water retention on surfaces with the effect decreasing with the increase in the angle, whereas a higher water contact angle (>90°) reduces the chances of water retention on surfaces, due to the ease of flow out [156]. As water molecules play significant roles in corrosion, the retention on corrosion vulnerable surfaces enhances the corrosion and deterioration of the materials. The water-repellent ability of this ZnO nanoparticle cum cashew nut shell liquid resin mixed paint could be attributed to the reduction of cardanol that has high hydrophilic characteristics [157] due to the reduced number of active surface hydroxyl group in the mix.

Application of nanomaterials for anti-reflective coating is an important source of energy conservation that plays an important role in light utilization efficiency, via minimization of light loss during transmission [158]. Hence, ensuring that optical surfaces efficiently conserve the energy available to them will improve the performance of devices used in solar cells and other light energy-dependent components. The use of micro-reactor-assisted nanomaterial deposition process to grow ZnO nanostructured anti-reflective coatings on Si substrate in an aqueous solution was used to exemplify the effect of nanostructures on reflectance suppression [116]. The authors used residual time, temperature, and concentration of precursor solution control to obtain a reflectance suppression of published silicon, between wavelengths of 400–900 nm from 10.6% to 3.4% by adding ZnO nanoparticles.

6.2 Nanostructure application in photovoltaic cells

Nanomaterials can improve the potency of solar cells by improving light trapping and photo-carrier collection abilities of devices used in photovoltaic cells [3].

Table 3: Summary of nanomaterials and nanostructure photovoltaic (PV) devices.

Type of nanomaterial	Remarks	References
Single nanowire PV devices	– Consist mainly of quasi-1-D materials such as nanowires, nanopillars, and nanotubes – This includes integrated, nanoelectronics, and photoelectronic materials – The materials have controllable carrier transport along the axis – Low efficiency of PV devices is due to the large surface-to-volume- ratio and high surface recombination of Si – Au catalyst used for the fabrication of Si nanowires in vapor-liquid-solid growth introduces impurities that affect the band gaps, deteriorate photon-carrier life cycle, and reduce PV device performance	[3, 158, 159]
Nanowire and nanopillar array PV devices	– Si, InP, CdS, GaAs, and ZnO have been used as active materials in the devices – Fabrication has been mainly by vapor-liquid-solid technique, dry etching, top-down etching, and photolithography – p-n junction-masked nanowire, microwire, and nanopillar devices have improved photon-carrier collection – Si-fabricated nanowires have increased efficiency in PV devices	[160, 161]
CdS, CdTe, and nanopillar thin-film PV devices	– CdS thin film and CdTe thin film have untreated surface recombination velocity of 10^8 cmS^{-1} and 10^4 cmS^{-1}, respectively – Alumina membranes have been used as template for fabricating these thin-film PV devices – Nanoimprint-assisted anodization process has been used to grow ordered hexagonal pore array of alumina membrane – Nanopillar solar fabrication can be implemented on bendable plastics for PV application	[3, 162]
Nanoparticles and quantum dot solar cells	– These nanomaterials are noted for unique properties such as size-dependent band gap and multi-excitation generation, which enables new PV mechanism to potentially break current thermodynamic limits – Compatible with solution-based process and can be fabricated using low temperature at low cost and high throughput	[3, 163, 164]

Nanostructures enhance the performance of photovoltaic performance by facilitating the photon-carrier collection via ensuring that the direction of light propagation is orthogonal on the carrier collection. Table 3 summarizes some of the nanostructures and nanomaterials that have been predominantly used for photovoltaic cells.

6.3 Gas-sensing application of nanostructures

Nanostructures have found excellent applications in gas sensing, due to the high specific area [165], change of resistance on exposure to gases [166], and high photoconduction abilities [167]. Different nanomaterials such as nanowires, nanoribbons, nanorods, nanotubes, and nanobelts made from ZnO, TiO_2, WO_3, In_2O_3, Fe_2O_3, CuO, NiO, Ga_2O_3, SnO_2, and V_2O_5 have typical characteristics that make them very good materials for gas-sensing application [168]. The work of numerous researchers has attested to the usability of the above-mentioned nanomaterials in gas sensing, as exemplified in literature [167, 169–171].

Exposing ZnO nanostructures to ambient gases that have oxidizing tendencies causes the surface of the material to adsorb the gas molecules, which captures an electron from the ZnO conduction band and causes an increase in the resistance of the material [167–169, 172]. The work of Pan et al. [167] on ZnO hierarchical nanostructures using the complementary metal oxide-semiconductor technique to form a patterned triple layer nanostructure was about 2800% more efficient for gas sensing than regularly used nanowire gas sensors. The researchers ensured a local growth of the ZnO hierarchical nanostructure on a single Si chip at ambient temperature using photolithography, physical vapor deposition, and lift-off. A Au catalyst contained in a triple-layer metal electrode in the fabrication of the nanostructure facilitated the reaction. Similarly, individual single-crystals of the SnO_2 nanoribbons sense NO_2 gas at room temperature due to the strong photoconduction abilities of the nanostructure, which resulted in electron trapping and adsorption of NO_2 and increasing of the conductivity of the nanoribbons [173]. Wang et al. [170] used three types of TiO_2 nanobelts – $Na_2Ti_3O_2$, $H_2Ti_3O_7$, and TiO_2 prepared by hydrothermal process to obtain nanobelts that were used for gas sensing. They connected the nanobelts with hydrogen bonds and bridged oxygen atoms to enhance their properties for gas sensing at sub part per billion (ppb) levels. As TiO_2 is an n-type semi-conductor [174], the concentration of oxygen in the nanobelt was affected by the oxygen partial pressure in the environment. This caused a higher resistance in the nanobelts due to the decrease in the density of the oxygen resulting from electron captured by the invading environmental oxygen. Furthermore, SnO_2 hierarchical nanostructures, prepared by the hydrothermal process, using stannous sulfate ($SnSO_4$) and trisodium citrate dihydrate ($Na_3C_6H_5O_7{\cdot}2H_2O$) in an ethanol-water system were used for testing butanol gas sensing ability by Zhang et al. [175]. The researchers affirmed that the nanostructure could sense butanol gas concentration from 1 to 200 ppm (parts per million) with a stable electrical signal over a period of 60 days. The sensing ability of the nanostructure was also attributed to the ability to absorb atmospheric oxygen, ionizing and capturing of free electrons from the SnO_2 conductance band per Eq. (20) [175].

$$\begin{cases} O_2(\text{gas}) + e^{-1} \rightarrow O_2^-(\text{ads}) \\ O_2^-(\text{ads}) + e^{-1} \rightarrow 2O^-(\text{ads}) \end{cases} \tag{20}$$

The presence of O_2^-(ads) and O^-(ads) ions on the nanocrystal of SnO_2 enhances the receptor functions of the nanostructure and its ability to sense gases as the exposition of sensors made with the material, which has a reducing ability, reacts with the molecules of the gas, absorbing oxygen, and releasing trapped electrons on the conductance band [171, 175, 176]. α-Fe_2O_3 nanotubes with uniform growth morphology have been shown to have a high specific area and exhibits good sensitivity to gases as well as excellent electrochemical characteristic that culminates in a discharge capability of 1415 $mAhS^{-1}$ at 100 mAS^{-1} and 20°C [15].

7 Conclusions

This research focused on the advances in nanotechnology as it applies to nanostructure characterization, nanofabrication, growth mechanism, and industrial application. The unique characteristics of nanostructures and nanomaterials, which includes high band gap, piezoelectrical, biocompatible, and pyroelectrical properties made them suitable for sensors, photoanodes, transistors, light-emitting diodes, lasers, and logic gate devices.

The use of different physical, chemical, and mechanical techniques such as the wet chemical method, electrodeposition, metal organic chemical deposition, flux method, molecular beam epitaxy, electrospinning, and sputtering have helped to develop unique nanostructures. These nanostructures that include nanowires, nanotubes, nanobelts, nanohelices, nanorings, nanocage, nanosheets, and nanorods have different orientations,

morphologies, and characteristics. Some of the specific characteristics of these nanostructures include better anti-reflectance, due to the high porosity of the nanostructures and increased optical absorption in near infrared. The enhanced anti-reflectance helps to increase the quantum efficiency of nanotubes. Increased photochemical performance of nanowires have resulted from enhanced charge dynamics and increased area of electrochemical reactions, whereas, photoanodic characteristics of the nanostructures have made them applicable in lithium-ion batteries, due to the high corrosion resistance, high thermal capability, and environmental friendliness.

The growth mechanism of nanostructures depends on factors such as temperature, diffusion rate, buffer layers and catalysts, surface energy, orientation, doping, and alloying. The existence of lattice mismatch, differential thermal expansion, and high deposition temperatures have been attributed to hetroepitaxy, which has resulted in the defects of nanostructures. Although heteroepitaxy has affected the characteristics of nanostructures, the study of the mechanism has potentially opened new frontiers in nanostructure application. Limited data and the complexities associated with the description of the physical growth of nanostructures necessitated the use of statistical, diffusion-deposition, and cross-domain models for nanostructure growth modeling. Preference has been given to nanowire length growth, morphology of the nanowires, and the local process conditions affecting the morphology of the nanowire in the system, in modeling the growth mechanism of nanowires on different substrates by the diffusion-deposition process.

Nanostructures such as ZnO, TiO_2, WO_3, In_2O_3, Fe_2O_3, CuO, NiO, Ga_2O_3, SnO_2, and V_2O_5 have found applications in gas sensing, due to the high specific area, change in resistance on exposure to gases, and high photoconduction abilities. Nanostructures are also excellent materials for solar photovoltaic cells, due to the photon-carrier collection abilities, anti-reflectance qualities that help to prevent loss of light energy, large-surface-to-volume ratio, high surface area recombination, size-dependent band gap, and multi-excitation generation. NIR reflective characteristics of nanostructures have made them find application in coating facilities used in military, construction, plastic, and petrochemical industries because of their ability to minimize corrosion degradation, minimize urban heat island effect, enhance the life cycle duration of facilities, enhance aesthetics, and minimize energy consumption.

Acknowledgment: This work is funded by the SUTD-ZJU Collaboration Research Grant ZJURP1500103 and the SUTD Start-Up Research Grant no. SRG-EPD-2015-108.

References

[1] Araneo R, Rinaldi A, Notargiacomo A, Pea M, Celozzi S. Advanced mechanical and electrical characterization of piezoelectric ZnO nanowires for electro-mechanical modeling of enhanced performance sensors. *Sens. Actuators A Phys*. 2016, 244, 166–173.

[2] Steeg E, Polzer F, Kirmse H, Qiao Y, Rabe JP, Kirstein S. Nucleation, growth, and dissolution of silver nanostructures formed in nanotubular J-aggregates of amphiphilic cyanine dyes. *J. Colloid Interface Sci*. 2016, 472, 187–194.

[3] Yu R, Lin Q, Leung SF, Fan Z. Nanomaterials and nanostructures for efficient light absorption and photovoltaics. *Nano Energy* 2012, 1, 57–72.

[4] Chaudhari S, Srinivasan M. 1D hollow α-Fe_2O_3 electrospun nanofibers as high performance anode material for lithium ion batteries. *J. Mater. Chem*. 2012, 22, 23049–23056.

[5] Li L, Xu C, Zhao Y, Ziegler KJ. Balancing surface area with electron recombination in nanowire-based dye-sensitized solar cells. *Sol. Energy* 2016, 132, 214–220.

[6] Zhang Q, Li H, Ma Y, Zhai T. ZnSe nanostructures: synthesis, properties and applications. *Prog. Mater. Sci*. 2016, 83, 472–535.

[7] Han J, Wang L, Guo R. Facile synthesis of hierarchical conducting polymer nanotubes derived from nanofibers and their application for controlled drug release. *Macromol. Rapid Commun*. 2011, 32, 729–735.

[8] Trung DQ, Tuan NT, Chung HV, Duong PH, Huy PT. On the origin of green emission in zinc sulfide nanowires prepared by a thermal evaporation method. *J. Lumin*. 2014, 153, 321–325.

[9] Wen X, Tang L. One-dimensional copolymer nanostructures loaded with silver nanoparticles fabricated via metallogel template copolymerization and their pH dependent photocatalytic degradation of methylene blue. *J. Mol. Catal. A Chem*. 2015, 399, 86–96.

[10] Abidian MR, Kim DH, Martin DC. Conducting-polymer nanotubes for controlled drug release. *Adv. Mater*. 2006, 18, 405–409.

[11] Cho SI, Lee SB. Fast electrochemistry of conductive polymer nanotubes: synthesis, mechanism, and application. *Acc. Chem. Res*. 2008, 41, 699–707.

[12] Ni W, Liang F, Liu J, Qu X, Zhang C, Li J, Wang Q, Yang Z. Polymer nanotubes toward gelating organic chemicals. *Chem. Commun*. 2011, 47, 4727–4729.

[13] Li FJ, Zhang S, Lee JW, Guo J, White TJ, Li B, Zhao D. Orientation of silicon nanowires grown from nickel-coated silicon wafers. *J. Cryst. Growth* 2014, 404, 26–33.

[14] Huang X, Zeng Z, Bao S, Wang M, Qi X, Fan Z, Zhang H. Solution-phase epitaxial growth of noble metal nanostructures on dispersible single-layer molybdenum disulfide nanosheets. *Nat. Commun*. 2013, 4, 1444.

[15] Zhang F, Yang H, Xie X, Li L, Zhang L, Yu J, Zhao H, Liu B. Controlled synthesis and gas-sensing properties of hollow sea urchin-like α-Fe_2O_3 nanostructures and α-Fe_2O_3 nanocubes. *Sens. Actuators B Chem*. 2009, 141, 381–389.

[16] Xu S, Wang ZL. One-dimensional ZnO nanostructures: solution growth and functional properties. *Nano Res*. 2011, 4, 1013–1098.

[17] Teichert C. Self-organization of nanostructures in semiconductor heteroepitaxy. *Phys. Rep*. 2002, 365, 335–432.

[18] Hetzl M, Schuster F, Winner A, Weiszer S, Stutzmann M. GaN nanowires on diamond. *Mater. Sci. Semicond. Process.* 2016, 48, 65–78.
[19] Mehta RJ, Zhang Y, Zhu H, Parker DS, Belley M, Singh DJ, Ramprasad R, Borca-Tasciuc T, Ramanath G. Seebeck and figure of merit enhancement in nanostructured antimony telluride by antisite defect suppression through sulfur doping. *Nano Lett.* 2012, 12, 4523–4529.
[20] Randhawa JS, Kanu LN, Singh G, Gracias DH. Importance of surface patterns for defect mitigation in three-dimensional self-assembly. *Langmuir* 2010, 26, 12534–12539.
[21] Phua CC, Chong TC, Lau WS. Improved crystalline quality of molecular beam epitaxy grown GaAs-on-Si epilayer through the use of low-temperature GaAs intermediate layer. *Jpn. J. Appl. Phys.* 1994, 33, L405.
[22] Lebedeva IV, Knizhnik AA, Bagatur'yants AA, Potapkin BV. Kinetics of 2D–3D transformations of carbon nanostructures. *Phys. E Low Dimens. Syst. Nanostruct.* 2008, 40, 2589–2595.
[23] Kohno H, Takeda S. Chains of crystalline-Si nanospheres: growth and properties. *e-J. Surf. Sci. Nanotechnol.* 2005, 3, 131–140.
[24] Li FJ, Zhang S, Lee JW, Zhao D. Wire or no wire–depends on the catalyst layer thickness. *J. Cryst. Growth* 2013, 381, 87–92.
[25] Xing YJ, Yu DP, Xi ZH, Xue ZQ. Silicon nanowires grown from Au-coated Si substrate. *Appl. Phys. A* 2003, 76, 551–553.
[26] Rurali R. Colloquium: structural, electronic, and transport properties of silicon nanowires. *Rev. Mod. Phys.* 2010, 82, 427.
[27] Wacaser BA, Deppert K, Karlsson LS, Samuelson L, Seifert W. Growth and characterization of defect free GaAs nanowires. *J. Cryst. Growth* 2006, 287, 504–508.
[28] Chen ZG, Ni A, Li F, Cong H, Cheng HM, Lu GQ. Synthesis and photoluminescence of tetrapod ZnO nanostructures. *Chem. Phys. Lett.* 2007, 434, 301–305.
[29] Li X. Metal assisted chemical etching for high aspect ratio nanostructures: a review of characteristics and applications in photovoltaics. *Curr. Opin. Solid State Mater. Sci.* 2012, 16, 71–81.
[30] Wang ZL. Zinc oxide nanostructures: growth, properties and applications. *J. Phys. Condens. Matter* 2004, 16, R829.
[31] Moore D, Wang ZL. Growth of anisotropic one-dimensional ZnS nanostructures. *J. Mater. Chem.* 2006, 16, 3898–3905.
[32] Xia Y, Yang P, Sun Y, Wu Y, Mayers B, Gates B, Yin Y, Kim F, Yan H. One-dimensional nanostructures: synthesis, characterization, and applications. *Adv. Mater.* 2003, 15, 353–389.
[33] Carter PW, Hillier AC, Ward MD. Nanoscale surface topography and growth of molecular crystals: the role of anisotropic intermolecular bonding. *J. Am. Chem. Soc.* 1994, 116, 944–953.
[34] Li Y, Bartelt MC, Evans JW, Waelchli N, Kampshoff E, Kern K. Transition from one-to two-dimensional island growth on metal (110) surfaces induced by anisotropic corner rounding. *Phys. Rev. B* 1997, 56, 12539.
[35] Sun C, Xue D. Tailoring anisotropic morphology at the nanoregime: surface bonding motif determines the morphology transformation of ZnO nanostructures. *J. Phys. Chem.* C, 2013, 117, 5505–5511.
[36] Jones MR, Macfarlane RJ, Lee B, Zhang J, Young KL, Senesi AJ, Mirkin CA. DNA-nanoparticle superlattices formed from anisotropic building blocks. *Nat. Mater.* 2010, 9, 913–917.
[37] Glotzer SC, Solomon MJ. Anisotropy of building blocks and their assembly into complex structures. *Nat. Mater.* 2007, 6, 557–562.
[38] Sacanna S, Irvine WTM, Chaikin PM, Pine DJ. Lock and key colloids. *Nature* 2010, 464, 575–578.
[39] Fang XS, Ye CH, Zhang LD, Wang YH, Wu YC. Temperature-controlled catalytic growth of ZnS nanostructures by the evaporation of ZnS nanopowders. *Adv. Funct. Mater.* 2005, 15, 63–68.
[40] Yin LW, Bando Y, Zhan JH, Li MS, Golberg D. Self-assembled highly faceted wurtzite-type ZnS single-crystalline nanotubes with hexagonal cross-sections. *Adv. Mater.* 2005, 17, 1972–1977.
[41] Wang ZL. Splendid one-dimensional nanostructures of zinc oxide: a new nanomaterial family for nanotechnology. *ACS Nano* 2008, 2, 1987–1992.
[42] Djurišić AB, Leung YH. Optical properties of ZnO nanostructures. *Small* 2006, 2, 944–961.
[43] Devarapalli RR, Shinde DR, Barka-Bouaifel F, Yenchalwar SG, Boukherroub R, More MA, Shelke MV. Vertical arrays of SiNWs–ZnO nanostructures as high performance electron field emitters. *J. Mater. Chem.* 2012, 22, 22922–22928.
[44] Djurišić AB, Ng AMC, Chen XY. ZnO nanostructures for optoelectronics: material properties and device applications. *Prog. Quantum Electron.* 2010, 34, 191–259.
[45] Shen GZ, Bando Y, Liu BD, Golberg D, Lee CJ. Characterization and field-emission properties of vertically aligned ZnO nanonails and nanopencils fabricated by a modified thermal-evaporation process. *Adv. Funct. Mater.* 2006, 16, 410–416.
[46] Padmanabhan SC, Ledwith D, Pillai SC, McCormack DE, Kelly JM. Microwave-assisted synthesis of ZnO micro-javelins. *J. Mater. Chem.* 2009, 19, 9250–9259.
[47] Fan HJ, Fuhrmann B, Scholz R, Himcinschi C, Berger A, Leipner H, Dadgar A, Krost A, Christiansen S, Gösele U, Zacharias M. Vapour-transport-deposition growth of ZnO nanostructures: switch between c-axial wires and a-axial belts by indium doping. *Nanotechnology* 2006, 17, S231.
[48] Schmidt-Mende L, MacManus-Driscoll JL. ZnO–nanostructures, defects, and devices. *Mater. Today* 2007, 10, 40–48.
[49] Demianets LN, Kostomarov DV, Kuz'mina IP, Pushko SV. Mechanism of growth of ZnO single crystals from hydrothermal alkali solutions. *Crystallogr. Rep.* 2002, 47, S86–S98.
[50] Wang H, Xie J, Yan K, Duan M. Growth mechanism of different morphologies of ZnO crystals prepared by hydrothermal method. *J. Mater. Sci. Technol.* 2011, 27, 153–158.
[51] Yamabi S, Imai H. Growth conditions for wurtzite zinc oxide films in aqueous solutions. *J. Mater. Chem.* 2002, 12, 3773–3778.
[52] Kawska A, Duchstein P, Hochrein O, Zahn D. Atomistic mechanisms of ZnO aggregation from ethanolic solution: ion association, proton transfer, and self-organization. *Nano Lett.* 2008, 8, 2336–2340.
[53] Navas MP, Soni RK, Tarasenka N, Tarasenko N. Temperature and solution assisted synthesis of anisotropic ZnO nanostructures by pulsed laser ablation. *Appl. Surf. Sci.* 2017, 414, 413–423.
[54] Watanabe M, Liu C, Hayashi K. Growth orientation control of metal nanostructures using linearly polarized light irradiation. *Thin Solid Films* 2017, 621, 137–144.
[55] Zhou F, Xin S, Liang HW, Song LT, Yu SH. Carbon nanofibers decorated with molybdenum disulfide nanosheets: synergistic lithium storage and enhanced electrochemical performance. *Angew. Chem. Int. Ed.* 2014, 53, 11552–11556.
[56] Huang KJ, Zhang JZ, Shi GW, Liu YM. Hydrothermal synthesis of molybdenum disulfide nanosheets as supercapacitors electrode material. *Electrochim. Acta* 2014, 132, 397–403.

[57] Novoselov KS, Geim AK, Morozov SV, Jiang D, Zhang Y, Dubonos SV, Grigorieva IV, Firsov AA. Electric field effect in atomically thin carbon films. *Science* 2004, 306, 666–669.
[58] Geim AK, Novoselov KS. The rise of graphene. *Nat. Mater.* 2007, 6, 183–191.
[59] Eda G, Fanchini G, Chhowalla M. Large-area ultrathin films of reduced graphene oxide as a transparent and flexible electronic material. *Nat. Nanotechnol*. 2008, 3, 270–274.
[60] Huang X, Yin Z, Wu S, Qi X, He Q, Zhang Q, Yan Q, Boey F, Zhang H. Graphene-based materials: synthesis, characterization, properties, and applications. *Small* 2011, 7, 1876–1902.
[61] Huang X, Zhou X, Wu S, Wei Y, Qi X, Zhang J, Boey F, Zhang H. Reduced graphene oxide-templated photochemical synthesis and *in situ* assembly of Au nanodots to orderly patterned Au nanodot chains. *Small* 2010, 6, 513–516.
[62] Zhu Y, Murali S, Cai W, Li X, Suk JW, Potts JR, Ruoff RS. Graphene and graphene oxide: synthesis, properties, and applications. *Adv. Mater*. 2010, 22, 3906–3924.
[63] Courty A, Henry AI, Goubet N, Pileni MP. Large triangular single crystals formed by mild annealing of self-organized silver nanocrystals. *Nat. Mater.* 2007, 6, 900–907.
[64] Kong YC, Yu DP, Zhang B, Fang W, Feng SQ. Ultraviolet-emitting ZnO nanowires synthesized by a physical vapor deposition approach. *Appl. Phys. Lett*. 2001, 78, 407–409.
[65] Pang Y, Liu Y, Gao M, Ouyang L, Liu J, Wang H, Zhu M, Pan H. A mechanical-force-driven physical vapour deposition approach to fabricating complex hydride nanostructures. *Nat. Commun*. 2014, 5, 3519.
[66] Yang JL, An SJ, Park WI, Yi GC, Choi W. Photocatalysis using ZnO thin films and nanoneedles grown by metal-organic chemical vapor deposition. *Adv. Mater*. 2004, 16, 1661–1664.
[67] Chen Y, Selvamanickam V, Zhang Y, Zuev Y, Cantoni C, Specht E, Paranthaman MP, Aytug T, Goyal A, Lee D. Enhanced flux pinning by BaZrO3 and (Gd, Y) 2O3 nanostructures in metal organic chemical vapor deposited GdYBCO high temperature superconductor tapes. *Appl. Phys. Lett.* 2009, 94, 062513.
[68] Yoshizawa M, Kikuchi A, Mori M, Fujita N, Kishino K. Growth of self-organized GaN nanostructures on Al2O3 (0001) by RF-radical source molecular beam epitaxy. *Jpn. J. Appl. Phys*. 1997, 36, L459.
[69] Dolbec R, El Khakani MA, Serventi AM, Trudeau M, Saint-Jacques RG. Microstructure and physical properties of nanostructured tin oxide thin films grown by means of pulsed laser deposition. *Thin Solid Films* 2002, 419, 230–236.
[70] Söderberg H, Odén M, Molina-Aldareguia JM, Hultman L. Nanostructure formation during deposition of TiN/SiN {sub x} nanomultilayer films by reactive dual magnetron sputtering. *J. Appl. Phys*. 2005, 97, 114327.
[71] Bognitzki M, Czado W, Frese T, Schaper A, Hellwig M, Steinhart M, Greiner A, Wendorff JH. Nanostructured fibers via electrospinning. *Adv. Mater*. 2001, 13, 70–72.
[72] Daraio C, Jin S. Synthesis and patterning methods for nanostructures useful for biological applications. In: Silva G., Parpura V. (eds) *Nanotechnology for Biology and Medicine*. Fundamental Biomedical Technologies. Springer: New York, 2012, pp. 27–44.
[73] Ma, C, Chen, C. *Pulsed Laser Deposition for Complex Oxide Thin Film and Nanostructure. Advanced Nano Deposition Methods*, John Wiley & Sons: Weinhelm, Germany, 2016.
[74] Chu SZ, Wada K, Inoue S, Todoroki SI, Takahashi YK, Hono K. Fabrication and characteristics of ordered Ni nanostructures on glass by anodization and direct current electrodeposition. *Chem. Mater*. 2002, 14, 4595–4602.
[75] Hu Y, Jin J, Wu P, Zhang H, Cai C. Graphene–gold nanostructure composites fabricated by electrodeposition and their electrocatalytic activity toward the oxygen reduction and glucose oxidation. *Electrochim. Acta* 2010, 56, 491–500.
[76] Jimenez-Cadena G, Comini E, Ferroni M, Vomiero A, Sberveglieri G. Synthesis of different ZnO nanostructures by modified PVD process and potential use for dye-sensitized solar cells. *Mater. Chem. Phys*. 2010, 124, 694–698.
[77] Liu L, Ning T, Ren Y, Sun Z, Wang F, Zhou W, Xie S, Song L, Luo S, Liu D, Shen J. Synthesis, characterization, photoluminescence and ferroelectric properties of $PbTiO_3$ nanotube arrays. *Mater. Sci. Eng. B* 2008, 149, 41–46.
[78] Liang L, Kang X, Sang Y, Liu H. One-dimensional ferroelectric nanostructures: synthesis, properties, and applications. *Adv. Sci.* 2016, 3, 1500358.
[79] Xie J, Xia Y. Electrospinning: an enabling technique for nanostructured materials. *Mater. Matter* 2008, 3, 19–23.
[80] Álvarez R, Garcia-Martin JM, Garcia-Valenzuela A, Macias-Montero M, Ferrer FJ, Santiso J, Rico V, Cotrino J, Gonzalez-Elipe AR, Palmero A. Nanostructured Ti thin films by magnetron sputtering at oblique angles. *J. Phys. D Appl. Phys*. 2015, 49, 045303.
[81] Yang SY, Jeon G, Kim JK. A high density array of free standing alumina nanotubes aligned vertically on solid substrates in a large area. *J. Mater. Chem*. 2012, 22, 23017–23021.
[82] Tseng PC, Yu P, Chen HC, Tsai YL, Han HW, Tsai MA, Chang CH, Kuo HC. Angle-resolved characteristics of silicon photovoltaics with passivated conical-frustum nanostructures. *Sol. Energy Mater. Sol. Cells* 2011, 95, 2610–2615.
[83] Tartaj P, Morales MP, Gonzalez-Carreño T, Veintemillas-Verdaguer S, Serna CJ. The iron oxides strike back: from biomedical applications to energy storage devices and photoelectrochemical water splitting. *Adv. Mater*. 2011, 23, 5243–5249.
[84] Docampo P, Guldin S, Steiner U, Snaith HJ. Charge transport limitations in self-assembled TiO_2 photoanodes for dye-sensitized solar cells. *J. Phys. Chem. Lett*. 2013, 4, 698–703.
[85] Pinaud BA, Vesborg PC, Jaramillo TF. Effect of film morphology and thickness on charge transport in Ta_3N_5/Ta photoanodes for solar water splitting. *J. Phys. Chem. C* 2012, 116, 15918–15924.
[86] Shelton CK, Epps III TH. Block copolymer thin films: characterizing nanostructure evolution with *in situ* X-ray and neuron scattering. *Polymer* 2016, 105, 545–561.
[87] Jeong JW, Park WI, Kim MJ, Ross CA, Jung YS. Highly tunable self-assembled nanostructures from a poly (2-vinylpyridine-b-dimethylsiloxane) block copolymer. *Nano Lett.* 2011, 11, 4095–4101.
[88] Cheng JY, Mayes AM, Ross CA. Nanostructure engineering by templated self-assembly of block copolymers. *Nat. Mater*. 2004, 3, 823–828.
[89] Noh SY, Sun K, Choi C, Niu M, Yang M, Xu K, Jin S, Wang D. Branched TiO_2/Si nanostructures for enhanced photoelectrochemical water splitting. *Nano Energy* 2013, 2, 351–360.
[90] Bandaru PR, Yamada H, Narayanan R, Hoefer M. Charge transfer and storage in nanostructures. *Mater. Sci. Eng. R Rep*. 2015, 96, 1–69.
[91] Hasegawa H, Sato T, Kasai S, Adamowicz B, Hashizume T. Dynamics and control of recombination process at semiconductor surfaces, interfaces and nano-structures. *Sol. Energy* 2006, 80, 629–644.

[92] Zhou C, Dun C, Wang K, Zhang X, Shi Z, Liu G, Hewitt CA, Qiao G, Carroll DL. General method of synthesis ultrathin ternary metal chalcogenide nanowires for potential thermoelectric applications. *Nano Energy* 2016, 30, 709–716.
[93] Leandri C, Saifi H, Guillermet O, Aufray B. Silicon thin films deposited on Ag (001): growth and temperature behavior. *Appl. Surf. Sci*. 2001, 177, 303–306.
[94] Wu D, Xu T, Shi Z, Tian Y, Li X. Construction of ZnTe nanowires/Si p–n heterojunctions for electronic and optoelectronic applications. *J. Alloys Compd.* 2016, 661, 231–236.
[95] Perea DE, Wijaya E, Lensch-falk JL, Hemesath ER, Lauhon LJ. Tomographic analysis of dilute impurities in semiconductor nanostructures. *J. Solid State Chem.* 2008, 181, 1642–1649.
[96] Sanaka K, Pawlis A, Ladd TD, Lischka K, Yamamoto Y. Indistinguishable photons from independent semiconductor nanostructures. *Phys. Rev. Lett*. 2009, 103, 053601.
[97] Fan Z, Ruebusch DJ, Rathore AA, Kapadia R, Ergen O, Leu PW, Javey A. Challenges and prospects of nanopillar-based solar cells. *Nano Res*. 2009, 2, 829–843.
[98] Piñero JC, Araújo D, Pastore CE, Gutierrez M, Frigeri C, Benali A, Lelièvre JF, Gendry M. Twins and strain relaxation in zinc-blende GaAs nanowires grown on silicon. *Appl. Surf. Sci*. 2017, 395, 195–199.
[99] Golan Y, Hodes G, Rubinstein I. Electrodeposited quantum dots. 3. Interfacial factors controlling the morphology, size, and epitaxy. *J. Phys. Chem*. 1996, 100, 2220–2228.
[100] Habas SE, Lee H, Radmilovic V, Somorjai GA, Yang P. Shaping binary metal nanocrystals through epitaxial seeded growth. *Nat. Mater*. 2007, 6, 692–697.
[101] Fan FR, Liu DY, Wu YF, Duan S, Xie ZX, Jiang ZY, Tian ZQ. Epitaxial growth of heterogeneous metal nanocrystals: from gold nano-octahedra to palladium and silver nanocubes. *J. Am. Chem. Soc*. 2008, 130, 6949–6951.
[102] Persson AI, Ohlsson BJ, Jeppesen S, Samuelson L. Growth mechanisms for GaAs nanowires grown in CBE. *J. Cryst. Growth* 2004, 272, 167–174.
[103] Fafard S, Wasilewski Z, McCaffrey J, Raymond S, Charbonneau S. InAs self-assembled quantum dots on InP by molecular beam epitaxy. *Appl. Phys. Lett*. 1996, 68, 991–993.
[104] Ponchet A, Le Corre A, L'haridon H, Lambert B, Salaün S. Relationship between self-organization and size of InAs islands on InP (001) grown by gas-source molecular beam epitaxy. *Appl. Phys. Lett*. 1995, 67, 1850–1852.
[105] Persson AI, Larsson MW, Stenström S, Ohlsson BJ, Samuelson L, Wallenberg LR. Solid-phase diffusion mechanism for GaAs nanowire growth. *Nat. Mater*. 2004, 3, 677–681.
[106] Kamins TI, Williams RS, Basile DP, Hesjedal T, Harris JS. Ti-catalyzed Si nanowires by chemical vapor deposition: microscopy and growth mechanisms. *J. Appl. Phys*. 2001, 89, 1008–1016.
[107] Zheng N, Huang Y, Sun W, Du X, Liu HY, Moody S, Gao J, Mai YW. *In-situ* pull-off of ZnO nanowire from carbon fiber and improvement of interlaminar toughness of hierarchical ZnO nanowire/carbon fiber hydrid composite laminates. *Carbon* 2016, 110, 69–78.
[108] Ding Y, Gao PX, Wang ZL. Catalyst-nanostructure interfacial lattice mismatch in determining the shape of VLS grown nanowires and nanobelts: a case of Sn/ZnO. *J. Am. Chem. Soc*. 2004, 126, 2066–2072.
[109] Li YF, Lin F, Xu B, Liu FQ, Ye XL, Ding D, Wang ZG. Influence of growth conditions on self-assembled InAs nanostructures grown on (001)InP substrate by molecular beam epitaxy. *J. Cryst. Growth* 2001, 223, 518–522.
[110] Marcu A, Trupina L, Zamani R, Arbiol J, Grigoriu C, Morante JR. Catalyst size limitation in vapor–liquid–solid ZnO nanowire growth using pulsed laser deposition. *Thin Solid Films* 2012, 520, 4626–4631.
[111] Chan JC, Tran H, Pattison JW, Rananavare SB. Facile pyrolytic synthesis of silicon nanowires. *Solid State Electron*. 202, 54, 1185–1191.
[112] Fanyao Q, Fonseca ALA, Nunes OAC. Intense field effects on hydrogen impurities in quantum dots. *J. Appl. Phys*. 1997, 82, 1236–1241.
[113] Han SY, Paul BK, Chang CH. Nanostructured ZnO as biomimetic anti-reflective coatings on textured silicon using a continuous solution process. *J. Mater. Chem*. 2012, 22, 22906–22912.
[114] Kim HW, Kim HS, Na HG, Yang JC, Kim SS, Lee C. Self-catalytic growth and characterization of composite (GaN, InN) nanowires. *Chem. Eng. J*. 2010, 165, 720–727.
[115] Fortuna SA, Wen J, Chun IS, Li X. Planar GaAs nanowires on GaAs (100) substrates: self-aligned, nearly twin-defect free, and transfer-printable. *Nano Lett*. 2008, 8, 4421–4427.
[116] Mikkelsen A, Eriksson J, Lundgren E, Andersen JN, Weissenrieder J, Seifert W. The influence of lysine on InP (001) surface ordering and nanowire growth. *Nanotechnology* 2005, 16, 2354.
[117] Cui Y, Lauhon LJ, Gudiksen MS, Wang J, Lieber CM. Diameter-controlled synthesis of single-crystal silicon nanowires. *Appl. Phys. Lett*. 2001, 78, 2214–2216.
[118] Wang CX, Hirano M, Hosono H. Origin of diameter-dependent growth direction of silicon nanowires. *Nano Lett*. 2006, 6, 1552–1555.
[119] Jagannathan H, Deal M, Nishi Y, Woodruff J, Chidsey C, McIntyre PC. Nature of germanium nanowire heteroepitaxy on silicon substrates. *J. Appl. Phys*. 2006, 100, 024318.
[120] Shan CX, Liu Z, Hark SK. CdSe nanowires with controllable growth orientations. *Appl. Phys. Lett*. 2007, 90, 193123.
[121] Baruah S, Dutta J. Hydrothermal growth of ZnO nanostructures. *Sci. Technol. Adv. Mater*. 2009, 10, 013001.
[122] Cesar I, Sivula K, Kay A, Zboril R, Grätzel M. Influence of feature size, film thickness, and silicon doping on the performance of nanostructured hematite photoanodes for solar water splitting. *J. Phys. Chem. C* 2008, 113, 772–782.
[123] Zhang Q, Liu SJ, Yu SH. Recent advances in oriented attachment growth and synthesis of functional materials: concept, evidence, mechanism, and future. *J. Mater. Chem*. 2009, 19, 191–207.
[124] Solans C, Izquierdo P, Nolla J, Azemar N, Garcia-Celma MJ. Nano-emulsions. *Curr. Opin. Colloid Interface Sci*. 2005, 10, 102–110.
[125] Zhang R, Khalizov A, Wang L, Hu M, Xu W. Nucleation and growth of nanoparticles in the atmosphere. *Chem. Rev*. 2011, 112, 1957–2011.
[126] Dalmaschio CJ, Ribeiro C, Leite ER. Impact of the colloidal state on the oriented attachment growth mechanism. *Nanoscale* 2010, 2, 2336–2345.
[127] Wooster TJ, Golding M, Sanguansri P. Impact of oil type on nanoemulsion formation and Ostwald ripening stability. *Langmuir* 2008, 24, 12758–12765.

[128] Lebovitz AH, Khait K, Torkelson JM. Stabilization of dispersed phase to static coarsening: polymer blend compatibilization via solid-state shear pulverization. *Macromolecules* 2002, 35, 8672–8675.
[129] Schwarz KW, Tersoff J. From droplets to nanowires:dynamics of vapor-liquid-solid growth. *Phys. Rev. Lett*. 2009, 102, 206101.
[130] Kukushkin SA, Osipov AV. Phase transitions and nucleation of catalytic nanostructures under the action of chemical, physical, and mechanical factors. *Kinet. Catal*. 2008, 49, 79–91.
[131] Gamalski AD, Ducati C, Hofmann S. Cyclic supersaturation and triple phase boundary dynamics in germanium nanowire growth. *J. Phys. Chem. C* 2011, 115, 4413–4417.
[132] Ratto F, Rosei F. Order and disorder in the heteroepitaxy of semiconductor nanostructures. *Mater. Sci. Eng. R Rep*. 2010, 70, 243–264.
[133] Lee ST, Chen S, Braunstein G, Feng X, Bello I, Lau WM. Heteroepitaxy of carbon on copper by high-temperature ion implantation. *Appl. Phys. Lett*. 1991, 59, 785–787.
[134] Alomari M, Dussaigne A, Martin D, Grandjean N, Gaquiere C, Kohn E. AlGaN/GaN HEMT on (111) single crystalline diamond. *Electron. Lett*. 2010, 46, 1.
[135] Felbinger JG, Chandra MVS, Sun Y, Eastman LF, Wasserbauer J, Faili F, Babic D, Francis D, Ejeckam F. Comparison of GaN HEMTs on diamond and SiC substrates. *IEEE Electron Device Lett*. 2007, 28, 948–950.
[136] Xu L, Wang L, Huang Q. Growth process modeling of semiconductor nanowires for scale-up of nanomanufacturing: a review. *IIE Trans*. 2015, 47, 274–284.
[137] Sun B, Fernandez M, Barnard A. Statistics, damned statistics and nanoscience–using data science to meet the challenge of nanomaterial complexity. *Nanoscale Horiz*. 2016, 1, 89–95.
[138] Huang Q. Integrated nanomanufacturing and nanoinformatics for quality improvement. *Growth* 2011, 160, 200.
[139] Aghdam FF, Liao H, Huang Q. Modeling interaction in nanowire growth process toward improved yield. *IEEE Trans. Autom. Sci. Eng*. 2015, 14, 1139–1149.
[140] Xu S, Adiga N, Ba S, Dasgupta T, Wu CJ, Wang ZL. Optimizing and improving the growth quality of ZnO nanowire arrays guided by statistical design of experiments. *ACS Nano* 2009, 3, 1803–1812.
[141] Dubrovskii VG, Xu T, Lambert Y, Nys JP, Grandidier B, Stievenard D, Chen W, Pareige P. Narrowing the length distribution of Ge nanowires. *Phys. Rev. Lett*. 2012, 108, 105501.
[142] Harmand JC, Glas F, Patriarche. Growth kinetics of a single InP 1–x As x nanowire. *Phys. Rev. B* 2010, 81, 235436.
[143] Lu YY, Cui H, Yang GW, Wang CX. Diameter-dependent or independent: toward a mechanistic understanding of the vapor–liquid–solid Si nanowire growth rate. *Nano Lett*. 2012, 12, 4032–4036.
[144] Sosina S, Dasgupta T, Huang Q. A stochastic graphene growth kinetics model. *J. R. Stat. Soc. Ser. C Appl. Stat*. 2016, 65, 705–729.
[145] Shafiei S, Nourbakhsh A, Ganjipour B, Zahedifar M, Vakili-Nezhaad G. Diameter optimization of VLS-synthesized ZnO nanowires, using statistical design of experiment. *Nanotechnology* 2007, 18, 355708.
[146] Wu J, Huang Q. Graphene growth process modeling: a physical-statistical approach. *Appl. Phys. A* 2014, 116, 1747–1756.
[147] Ruth V, Hirth JP. Kinetics of diffusion-controlled whisker growth. *J. Chem. Phys*. 1964, 41, 3139–3149.
[148] Dubrovskii VG, Hervieu YY. Diffusion-induced growth of nanowires: generalized boundary conditions and self-consistent kinetic equation. *J. Cryst. Growth* 2014, 401, 431–440.
[149] Wali Q, Fakharuddin A, Yasin A, Ab Rahim MH, Ismail J, Jose R. One pot synthesis of multi-functional tin oxide nanostructures for high efficiency dye-sensitized solar cells. *J. Alloys Compd*. 2015, 646, 32–39.
[150] Xu X, Sun B, Berman PR, Steel DG, Bracker AS, Gammon D, Sham LJ. Coherent optical spectroscopy of a strongly driven quantum dot. *Science* 2007, 317, 929–932.
[151] Reithmaier JP, Sek G, Loffler A, Hofmann C, Kuhn S, Reitzenstein S, Keldysh LV, Kulakovskii VD, Reinecke TL, Forchel A. Strong coupling in a single quantum dot semiconductor microcavity system. *Nature* 2004, 432, 197–200.
[152] Badolato A, Hennessy K, Atature M, Dreiser J, Hu E, Petroff PM, Imamoğlu A. Deterministic coupling of single quantum dots to single nanocavity modes. *Science* 2005, 308, 1158–1161.
[153] Fang V, Kenedy J, Futter J, Manning J. A review of infrared reflectance properties of metal oxide nanostructures, GNS Science Report 2013/39. 23 p. 2013. Retrieved from https://www.gns.cri.nz/static/pubs/2013/SR%202013-039.pdf. 13/3/17.
[154] Balanand S, Maria MJ, Rajan TPD, Peer Mohamed A, Ananthakumar S. Bulk processing of ZnO nanostructures via microwave assisted oxidation of mechanically seeded Zn dust for functional paints and coatings. *Chem. Eng. J*. 2016, 284, 657–667.
[155] Echeverría M, Abreu CM, Deive FJ, Sanromán MA, Rodríguez A. Ionic liquids improve the anticorrosion performance of Zn-rich coatings. *RSC Adv*. 2014, 4, 59587–59593.
[156] Mohamed AM, Abdullah AM, Younan NA. Corrosion behavior of superhydrophobic surfaces: a review. *Arab. J. Chem*. 2015, 8, 749–765.
[157] Balachandran VS, Jadhav SR, Vemula PK, John G. Recent advances in cardanol chemistry in a nutshell: from a nut to nanomaterials. *Chem. Soc. Rev*. 2013, 42, 427–438.
[158] Tian B, Zheng X, Kempa TJ, Fang Y, Yu N, Yu G, Huang J, Lieber CM. Coaxial silicon nanowires as solar cells and nanoelectronic power sources. *Nature* 2007, 449, 885–889.
[159] Kempa TJ, Tian B, Kim DR, Hu J, Zheng X, Lieber CM. Single and tandem axial pin nanowire photovoltaic devices. *Nano Lett*. 2008, 8, 3456–3460.
[160] Kelzenberg MD, Turner-Evans DB, Putnam MC, Boettcher SW, Briggs RM, Baek JY, Lewis NS, Atwater HA. High-performance Si microwire photovoltaics. *Energy Environ. Sci*. 2011, 4, 866–871.
[161] Colombo C, Heiss M, Grätzel M, Fontcuberta MA. Gallium arsenide pin radial structures for photovoltaic applications. *Appl. Phys. Lett*. 2009, 94, 173108 (EPFL-ARTICLE-148563).
[162] Fan Z, Razavi H, Do JW, Moriwaki A, Ergen O, Chueh YL, Leu PW, Ho JC, Takahashi T, Reichertz LA, Neale S. Three-dimensional nanopillar-array photovoltaics on low-cost and flexible substrates. *Nat. Mater*. 2009, 8, 648–653.
[163] Corwine CR, Pudov AO, Gloeckler M, Demtsu SH, Sites JR. Copper inclusion and migration from the back contact in CdTe solar cells. *Sol. Energy Mater. Sol. Cells* 2004, 82, 481–489.
[164] Hou WW, Bob B, Li SH, Yang Y. Low-temperature processing of a solution-deposited CuInSSe thin-film solar cell. *Thin Solid Films* 2009, 517, 6853–6856.
[165] Chen J, Xu L, Li W, Gou XL. α-Fe_2O_3 nanotubes in gas sensor and lithium-ion battery applications. *Adv. Mater*. 2005, 17, 582–586.

[166] Wang D, Hu P, Xu J, Dong X, Pan Q. Fast response chlorine gas sensor based on mesoporous SnO_2. *Sens. Actuators B Chem.* 2009, 140, 383–389.
[167] Pan X, Zhao X, Chen J, Bermak A, Fan Z. A fast-response/recovery ZnO hierarchical nanostructure based gas sensor with ultra-high room-temperature output response. *Sens. Actuators B Chem*. 2015, 206, 764–771.
[168] Choi KJ, Jang HW. One-dimensional oxide nanostructures as gas-sensing materials: review and issues. *Sensors* 2010, 10, 4083–4099.
[169] Zhang SB, Wei SH, Zunger A. Intrinsic n-type versus p-type doping asymmetry and the defect physics of ZnO. *Phys. Rev. B* 2001, 63, 075205.
[170] Wang Y, Du G, Liu H, Liu D, Qin S, Wang N, Hu C, Tao X, Jiao J, Wang J, Wang ZL. Nanostructured Sheets of TiO_2 nanobelts for gas sensing and antibacterial applications. *Adv. Funct. Mater*. 2008, 18, 1131–1137.
[171] Patil LA, Shinde MD, Bari AR, Deo VV. Highly sensitive and quickly responding ultrasonically sprayed nanostructured SnO_2 thin films for hydrogen gas sensing. *Sens. Actuators B Chem*. 2009, 143, 270–277.
[172] Sun ZP, Liu L, Zhang L, Jia DZ. Rapid synthesis of ZnO nano-rods by one-step, room-temperature, solid-state reaction and their gas-sensing properties. *Nanotechnology* 2006, 17, 2266.
[173] Law M, Kind H, Messer B, Kim F, Yang PD. Photochemical sensing of NO_2 with SnO_2 nanoribbon nanosensors at room temperature. *Angew. Chem. Int. Ed.* 2002, 41, 2405–2408.
[174] Forro L, Chauvet O, Emin D, Zuppiroli L, Berger H, Levy F. High mobility n-type charge carriers in large single crystals of anatase (TiO_2). *J. Appl. Phys*. 1994, 75, 633–635.
[175] Zhang H, He Q, Zhu X, Pan D, Deng X, Jiao Z. Surfactant-free solution phase synthesis of monodispersed SnO_2 hierarchical nanostructures and gas sensing properties. *CrystEngComm* 2012, 14, 3169–3176.
[176] Xue X, Chen Z, Ma C, Xing L, Chen Y, Wang Y, Wang T. One-step synthesis and gas-sensing characteristics of uniformly loaded Pt@ SnO_2 nanorods. *J. Phys. Chem. C* 2010, 114, 3968–3972.

Bionotes

Chinedu I. Ossai
Engineering Product Development Pillar, Singapore University of Technology and Design, Singapore 487372, Singapore
chinedu_ossai@sutd.edu.sg

Chinedu I. Ossai is a Postdoctoral Research Fellow at the Singapore University of Technology and Design (SUTD) in the Engineering Product Development (EPD) pillar. He obtained his PhD in Mechanical Engineering from Curtin University, Perth, Australia, in 2016. His research interest is in stochastic modeling of nanodevice physics of failure and uncertainty quantification, development of reliability framework for asset prognostics and system health management, estimation of the reliability and remaining useful life of dynamic systems using machine learning as well as data analytics. To date, he has published over 19 articles in reputable peer-reviewed journals.

Nagarajan Raghavan
Engineering Product Development Pillar, Singapore University of Technology and Design, Singapore 487372, Singapore
nagarajan@sutd.edu.sg

Nagarajan Raghavan is an Assistant Professor at the Singapore University of Technology and Design (SUTD) in the Engineering Product Development (EPD) pillar. He obtained his PhD (Microelectronics, 2012) at the Division of Microelectronics, Nanyang Technological University (NTU). His work focuses on statistical characterization and reliability modeling of dielectric breakdown, application of Bayesian inference for nanomanufacturing, prognostics and health management, design for reliability and reliability statistics. He has authored/co-authored more than 120 peer-reviewed journal and conference articles as well as four book chapters.